Medical Image Registration and Interpolation by Optical Flow with Maximal Rigidity

Stephen L. Keeling[*] and Wolfgang Ring[†]

Abstract. In this paper a variational method for registering or mapping like points in medical images is proposed and analyzed. The proposed variational principle penalizes a departure from rigidity and thereby provides a natural generalization of strictly rigid registration techniques used widely in medical contexts. Difficulties with finite displacements are elucidated, and alternative infinitesimal displacements are developed for an optical flow formulation which also permits image interpolation. The variational penalty against non-rigid flows provides sufficient regularization for a well-posed minimization and yet does not rule out irregular registrations corresponding to an object excision. Image similarity is measured by penalizing the variation of intensity along optical flow trajectories. The approach proposed here is also independent of the order in which images are taken. For computations, a lumped finite element Eulerian discretization is used to solve for the optical flow. Also, a Lagrangian integration of the intensity along optical flow trajectories has the advantage of prohibiting diffusion among trajectories which would otherwise blur interpolated images. The subtle aspects of the methods developed are illustrated in terms of simple examples, and the approach is finally applied to the registration of magnetic resonance images.

1 Introduction

The diagnostic use of medical image sets in a clinical setting implicitly requires a point by point correspondence between the same tissue sites in separate images. For example, two given images may be of a single patient at different times, such as during a mammography examination involving repeated imaging after the injection of a contrast agent [26]. On the other hand, the images may be of a single patient viewed by different imaging modalities, such as by magnetic resonance and computerized tomography to provide complementary information for image-guided surgery [11]. In fact, images of two separate patients may even be compared to evaluate the extent of pathology of one in relation to the other [29]. Similarly, an image of a patient may be compared to an idealized atlas in order to identify or segment tissue classes based upon a detailed segmentation of the atlas [29]. Thus, what is needed finally is an explicit coordinate transformation that will map any point in one image to its corresponding point in the other. With such a mapping, images are said to be *registered.*

Since the term registration is often used rather loosely in the context of its applications, it may be useful to elaborate on the above description of what registration is by stating what it is not. Note that by manipulating intensities alone, it is possible to warp or morph one image to another without having an explicit coordinate transformation identifying like image points. Thus image registration is not image morphing, but can be used for such an application. Similarly, image interpolation can be achieved without registration, but a parameterized coordinate transformation can be used to interpolate between images. Also, when complementary information in separate imaging modalities is superimposed, images are said to be *fused.* Since fusion too can be achieved by manipulating intensities alone, fused images need not be registered, but rather *can* be fused by registration.

Rigid registration is performed under the constraint that images are related by a pure rigid-body transformation, i.e., a translation plus a rotation. Such registration is attractive in medical imaging because of the ubiquity of nearly rigid objects in the body. It is especially popular

---

[*] Institut für Mathematik, Karl-Franzens-Universität Graz, Heinrichstraße 36, 8010 Graz, Austria; email: stephen.keeling@uni-graz.at; tel: +43–316–380–5156; fax: +43–316–380–9815. Supported by the Fonds zur Förderung der wissenschaftliche Forschung under SFB 03, “Optimierung und Kontrolle”.

[†] Institut für Mathematik, Karl-Franzens-Universität Graz, Heinrichstraße 36, 8010 Graz, Austria; email: wolfgang.ring@uni-graz.at; tel: +43–316–380–5161; fax: +43–316–380–9815. Supported by the Fonds zur Förderung der wissenschaftliche Forschung under SFB 03, “Optimierung und Kontrolle”.

for image modality fusion in order to guide brain surgery [11]. Particularly when performed prospectively with the use of extrinsic fiducial markers, rigid registration and its concomitant errors are well understood [12]. Since rigid registration is widely used and treated as a standard for comparison in the medical community [11], even in cases for which a more flexible registration is sought [26], it was an initial aim of the present work to define a generalization which maximizes rigidity in a natural sense.

A leading application and demand for non-rigid registration is for mammographic image sequences in which tissue deformations are less rigid and more elastic [26]. This observation has motivated the development of registration methods based on linear elasticity [10], [24]. Alternatives emerge from noting that a rigid transformation is equivalent to one which is both conformal (angle preserving) and isometric (area preserving) [6]. Some authors relax rigidity by constraining transformations to be conformal or isometric [13]. Others employ a local rigidity constraint [19] or allow identified objects to move as rigid bodies [20]. The approach developed here involves instead a variational principle penalizing a departure from rigidity. Thus, a rigid registration is selected when one fits the data. Otherwise rigidity is maximized strongly or weakly depending upon the dominance of the rigidity penalty. Based upon a function space minimization, this approach is non-parametric. By contrast, many other non-rigid registration methods are parametric, based for instance upon the determination of polynomial coefficients [26].

Whether parametric or non-parametric, the unknowns in a registration problem are generally over-determined by the available information, and must be determined by optimizing an image similarity measure; see [11] for further details. In particular, it is a noteworthy conclusion of the study in [34] that highly accurate rigid registrations of multi-modal brain images can be achieved with information-theoretic measures. Nevertheless, as recognized in [25], mutual information contains no local spatial information, and random pixel perturbations leave underlying entropies unchanged. Thus, in the present framework image similarity is driven by penalizing the variation of a local image feature along trajectores connecting like points. In this introductory work, that local image feature is simply the raw intensity, but other discussed features can be treated naturally.

Because image registration is an ill-posed process, it can lead to quite aberrant results unless regularization is applied [9], [21]. In the approach developed here, a variational penalty on the departure from rigidity provides sufficient regularization for a well-posed minimization. At the same time, the penalty does not rule out irregular registrations, for example, corresponding to an object excision.

The approach developed in this work was influenced by Thirion's interpretation of optical flow as a means of driving a diffusion process in which one image is deformed toward a match with a static second image [28]. This process may be visualized in Fig. 1 with the deformations evolving from the front face (shown right) toward the back face (shown left) of the displayed box. Because of an apparent unnatural directionality in this diffusion process, the present work was oriented from the outset so that the registration would be the same independent of the order in which images are taken; see also [4]. With this preconception, one might already anticipate an elliptic formulation in the box of Fig. 1, with the given images imposed as boundary conditions on the front and back faces. In fact, an elliptic system is derived here for an optical flow field whose integrated trajectories connect like image points in the front and back faces. Natural boundary conditions also permit trajectories to leave the computational domain, which is a necessary condition to support purely rigid transformations. Furthermore, image interpolation is achieved in parallel image planes by distributing the intensity with minimal variation along trajectories. Thus, the optical flow is determined in an Eulerian frame and the intensity in a Lagrangian frame. Note that optical flow has been proposed in other ways for registration: with an evolution equation formulation that depends upon the order of the images [2], with more usual optical flow regularization that leads to aqueous effects which are unnatural for medical applications [15], and as a linearization of the nonlinear similarity criterion [19].

The paper can now be summarized as follows. In Section 2 a framework used throughout the paper is presented. Specifically, optical flow is defined and image similarity is developed in terms of the variation of intensity along optical flow trajectories. In Section 3 basic elements from elasticity theory are explored for registration regularization. It is shown that linearized elastic potential energy of finite displacements does not select rigid transformations preferentially, and that the unlinearized energy is computationally intractable. Finally, a computationally convenient penalty on the departure of infinitesimal displacements from rigidity is identified. Section 4 begins with a complete definition of the proposed variational registration method. Then the optimality conditions are derived separately for each variable in subsections. Simple examples are also considered to justify the choice of penalty functions and of boundary conditions. Also, the optical flow system is shown to be well-posed under the condition that the intensity does not manifest certain trivial symmetries. Section 5 begins by introducing the numerical framework for the proposed registration method. Then the discretizations of the optimality system of the previous section are developed separately for each variable in subsections. In Section 6 the final numerical implementation is applied both to test cases and to magnetic resonance images. In particular it is shown that the approach succeeds in achieving a natural generalization of rigid registration.

2 Image Similarity

Following the illustration in Fig. 1 for 2D images, let two given images I_0 and I_1 be situated respectively on the front and back faces of a box,

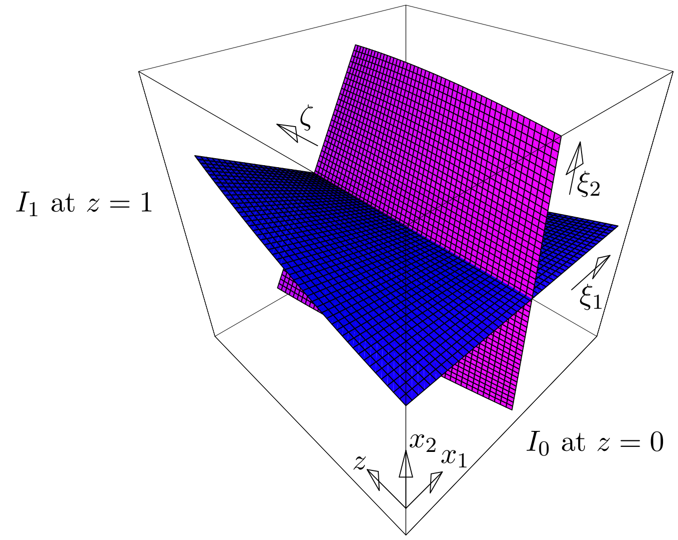

Figure 1: The domain Q with 2D images I_0 and I_1 on the front and back faces Ω_0 and Ω_1, respectively. Curvilinear coordinates are defined to be constant on trajectories connecting like points in I_0 and I_1.

$$Q = \{(x_1, \ldots, x_N, z) = (\boldsymbol{x}, z) : 0 < x_1, \ldots, x_N, z < 1\}, \tag{2.1}$$

i.e.,

$$I_0 \text{ on } \Omega_0 = \{(\boldsymbol{x}, z) \in \partial Q : z = 0\} \tag{2.2}$$

and

$$I_1 \text{ on } \Omega_1 = \{(\boldsymbol{x}, z) \in \partial Q : z = 1\}. \tag{2.3}$$

Then define curvilinear coordinates $(\xi_1, \ldots, \xi_N, \zeta) = (\boldsymbol{\xi}, \zeta)$ so that $\boldsymbol{\xi}$ is constant along trajectories through Q that connect like points in I_0 and I_1, and $\zeta = z$. Also, suppose that $\boldsymbol{x} = \boldsymbol{\xi}$ in Ω_0 and therefore the displacement vector within Q is $\boldsymbol{d} = \boldsymbol{x} - \boldsymbol{\xi}$. Further, a trajectory tangent is given by $(u_1, \ldots, u_N, 1)$ in terms of the optical flow defined as

$$\boldsymbol{u} = (u_1, \ldots, u_N) = \boldsymbol{x}_\zeta. \tag{2.4}$$

Now the simplest similarity measure discussed in [11], i.e., the sum of squared intensity differences, takes the following form,

$$\int_{\Omega_0^{\mathrm{c}}} [I_0(\boldsymbol{\xi}) - I_1(\boldsymbol{x}(\boldsymbol{\xi}, 1))]^2 \, d\boldsymbol{\xi}. \tag{2.5}$$

It is not assumed that every point in Ω_0 finds a like point in Ω_1, i.e., trajectories are allowed to move out of the box Q. Therefore, the domain of integration in (2.5) is given by $\Omega_0^{\mathrm{c}} = \{\boldsymbol{\xi} \in \Omega_0 : \boldsymbol{x}(\boldsymbol{\xi}, \zeta) \in Q, 0 < \zeta < 1\}$, the subset of Ω_0 on which trajectories extend completely through the full depth of Q. To reach a similarity measure which involves only infinitesimal displacements as opposed to the finite displacement $\boldsymbol{d}(\boldsymbol{\xi}, 1) = \boldsymbol{x}(\boldsymbol{\xi}, 1) - \boldsymbol{\xi}$, consider now the integral,

$$J_{\mathrm{s}}(I) = \int_0^1 \int_{\Omega_0^{\mathrm{c}}} \left[\frac{dI}{d\zeta}(\boldsymbol{x}(\boldsymbol{\xi}, \zeta), \zeta) \right]^2 d\boldsymbol{\xi} d\zeta, \tag{2.6}$$

constrained by the boundary conditions:

$$I(\boldsymbol{\xi}, 0) = I_0(\boldsymbol{\xi}), \quad I(\boldsymbol{x}(\boldsymbol{\xi}, 1), 1) = I_1(\boldsymbol{x}(\boldsymbol{\xi}, 1)), \qquad \boldsymbol{\xi} \in \Omega_0^{\mathrm{c}}. \tag{2.7}$$

To demonstrate the relation between (2.5) and (2.6), consider that, under the condition (2.7), $J_{\mathrm{s}}(I)$ is minimized by:

$$I(\boldsymbol{x}(\boldsymbol{\xi}, \zeta), \zeta) = I_0(\boldsymbol{\xi}) + \zeta[I_1(\boldsymbol{x}(\boldsymbol{\xi}, 1)) - I_0(\boldsymbol{\xi})]. \tag{2.8}$$

Substituting this expression into (2.6) then leads back to (2.5). However, with (2.4) the optical flow equation [16]:

$$\frac{dI}{d\zeta}(\boldsymbol{x}(\boldsymbol{\xi}, \zeta), \zeta) = \nabla_{\boldsymbol{x}} I \cdot \boldsymbol{x}_\zeta + I_\zeta = \nabla_{\boldsymbol{x}} I \cdot \boldsymbol{u} + I_z, \tag{2.9}$$

now suggests the following modification of (2.6),

$$\int_Q [\nabla_{\boldsymbol{x}} I \cdot \boldsymbol{u} + I_z]^2 \, d\boldsymbol{x} dz, \tag{2.10}$$

which has an integrand involving purely local information throughout Q. It differs from (2.6) by not including the transformation Jacobian $1/\det(\nabla_{\boldsymbol{\xi}} \boldsymbol{x})$. In other words, (2.10) gives a convenient *Eulerian* (local) counterpart to the *Lagrangian* (trajectory following) form appearing in (2.6). Furthermore, the counterpart to (2.7) in the Eulerian context is given by:

$$I = I_0 \text{ on } \Omega_0, \qquad I = I_1 \text{ on } \Omega_1. \tag{2.11}$$

It is also shown by a consideration of optimality conditions in Section 4 that a minimizer I for (2.10) should satisfy the supplementary boundary condition:

$$I = 0 \ \text{ on } \ \Gamma = \partial Q \backslash \{\Omega_0 \cup \Omega_1\}. \tag{2.12}$$

Thus, an image similarity measure is given by (2.10) under the constraints (2.11) and (2.12).

Other similarity measures can be treated along the same lines. Specifically, suppose $\mathcal{D}$ is an operator which extracts a local image feature which should differ as little as possible between like points in the images I_0 and I_1. Then subject to the new boundary conditions,

$$I = \mathcal{D} I_0 \text{ on } \Omega_0, \qquad I = \mathcal{D} I_1 \text{ on } \Omega_1, \tag{2.13}$$

the function I in (2.10) transports the chosen feature along optical flow trajectores. For instance, considered operators $\mathcal{D}$ include intensity scaling as well as differential operators designed to match level curves. Of course, other differential geometric or statistical descriptors can be treated naturally. However, (2.13) is not considered here in detail.

3 Elastic Regularization

For a given ζ in Fig. 1, consider now the deformation $\boldsymbol{x}(\boldsymbol{\xi},\zeta)$ and the associated matrix (the right Cauchy-Green strain tensor in elasticity [6]),

$$C(\zeta) = \nabla_{\boldsymbol{\xi}}\boldsymbol{x}^{\mathrm{T}}\nabla_{\boldsymbol{\xi}}\boldsymbol{x} = \{\nabla_{\boldsymbol{\xi}}x_i \cdot \nabla_{\boldsymbol{\xi}}x_j\}. \tag{3.1}$$

The transformation is conformal if $\nabla_{\boldsymbol{\xi}}x_i \cdot \nabla_{\boldsymbol{\xi}}x_j = 0$, $i \neq j$, and additionally isometric if $\|\nabla_{\boldsymbol{\xi}}x_i\|^2 = 1$, $i = 1,\dots,N$, and so rigid when $C(\zeta) = I$ [6]. Thus, the (Green-St.Venant) strain $E = \frac{1}{2}(C - I)$ measures how close the deformation is to being rigid. The work required to perform a given deformation gives the elastic potential energy stored in the deformed body [6],

$$W(E) = \int_{\Omega_0^c} \left[\lambda \mathrm{tr}(E)^2 + 2\mu|E|^2\right] d\boldsymbol{\xi}, \tag{3.2}$$

where λ and μ are the so-called Lamé constants [6]. Here, $|E|^2 = E : E$ where $:$ denotes a componentwise matrix scalar product. Now in terms of the displacement $\boldsymbol{d} = \boldsymbol{x} - \boldsymbol{\xi}$ the strain can be linearized according to $2E = C - I = \nabla_{\boldsymbol{\xi}}\boldsymbol{d} + \nabla_{\boldsymbol{\xi}}\boldsymbol{d}^{\mathrm{T}} + \nabla_{\boldsymbol{\xi}}\boldsymbol{d}^{\mathrm{T}}\nabla_{\boldsymbol{\xi}}\boldsymbol{d} \approx \nabla_{\boldsymbol{\xi}}\boldsymbol{d} + \nabla_{\boldsymbol{\xi}}\boldsymbol{d}^{\mathrm{T}}$ which gives the approximation to the elastic potential energy,

$$W(E) \approx \int_{\Omega_0^c} \left[\lambda(\nabla_{\boldsymbol{\xi}} \cdot \boldsymbol{d})^2 + \tfrac{1}{2}\mu\left|\nabla_{\boldsymbol{\xi}}\boldsymbol{d}^{\mathrm{T}} + \nabla_{\boldsymbol{\xi}}\boldsymbol{d}\right|^2\right] d\boldsymbol{\xi}. \tag{3.3}$$

With (2.5) and (3.3), consider (tentatively) computing a registration by minimizing the following cost,

$$\begin{aligned} J_{\mathrm{lin}}(\boldsymbol{d}) &= \int_{\Omega_0^c} \left[I_0(\boldsymbol{\xi}) - I_1(\boldsymbol{\xi} + \boldsymbol{d}(\boldsymbol{\xi},1))\right]^2 d\boldsymbol{\xi} \\ &+ \int_0^1 \int_{\Omega_0^c} \left[\lambda\left(\nabla_{\boldsymbol{\xi}} \cdot \boldsymbol{d}\right)^2 + \frac{\mu}{2}\left|\nabla_{\boldsymbol{\xi}}\boldsymbol{d}^{\mathrm{T}} + \nabla_{\boldsymbol{\xi}}\boldsymbol{d}\right|^2\right] d\boldsymbol{\xi} d\zeta. \end{aligned} \tag{3.4}$$

The following reasoning shows that (3.3) is not a suitable regularization for selecting rigid transformations. Suppose I_0 and I_1 are related by a rigid transformation $\boldsymbol{r}$ via $I_0(\boldsymbol{\xi}) = I_1(\boldsymbol{r}(\boldsymbol{\xi}))$. Clearly the choice of a morphing $\boldsymbol{x}(\boldsymbol{\xi},\zeta)$ in which $\boldsymbol{r}$ can be embedded via $\boldsymbol{x}(\boldsymbol{\xi},0) = \boldsymbol{\xi}$ and $\boldsymbol{x}(\boldsymbol{\xi},1) = \boldsymbol{r}(\boldsymbol{\xi})$ is not unique. Specifically, define the rigid-body motion $\hat{\boldsymbol{x}}(\boldsymbol{\xi},\zeta) = R(\zeta)(\boldsymbol{\xi}-\boldsymbol{a})+\boldsymbol{a}$, where $\boldsymbol{a}$ is the center of rotation and $R(\zeta) = e^{\zeta W}$ for a skew-symmetrix matrix W [22]. Also define the convex combination $\tilde{\boldsymbol{x}}(\boldsymbol{\xi},\zeta) = (1-\zeta)\boldsymbol{\xi}+\zeta\hat{\boldsymbol{x}}(\boldsymbol{\xi},1)$, which with increasing ζ corresponds to compressing the initial image and then expanding it to the final image. Assume further that the intensities corresponding to these transformations are given in Q by (2.8) with $\boldsymbol{x}$ replaced by $\hat{\boldsymbol{x}}$ and $\tilde{\boldsymbol{x}}$ respectively. With this choice, the similarity term (2.5) is zero. Now, with $\hat{\boldsymbol{d}} = \hat{\boldsymbol{x}}-\boldsymbol{\xi}$ and $\tilde{\boldsymbol{d}} = \tilde{\boldsymbol{x}} - \boldsymbol{\xi}$, an elementary calculation shows that $J_{\mathrm{lin}}(\tilde{\boldsymbol{d}}) < J_{\mathrm{lin}}(\hat{\boldsymbol{d}})$. In other words, the linearized elastic potential energy regularization selects the compression/expansion instead of the rigid-body motion.

The situation is different for the unlinearized elastic potential energy. If a cost functional J_{unl} is constructed with (2.5) and (3.2) analogously to (3.4), the unlinearized elastic potential energy regularization selects the rigid-body motion instead of the compression/expansion. However, the optimality system for J_{unl} is very complex and contains coefficients with terms $(\|\nabla_{\boldsymbol{\xi}}x_i\|^2 - 1)$ whose signs may not even be uniform.

Nevertheless, these difficulties can be circumvented by formulating rigidity in an Eulerian frame instead of in a Lagrangian frame. To this end, note that $\boldsymbol{x}_\zeta(\boldsymbol{\xi},\zeta) = \boldsymbol{u}(\boldsymbol{x}(\boldsymbol{\xi},\zeta),\zeta)$ gives $\nabla_{\boldsymbol{\xi}}\boldsymbol{x}_\zeta = \nabla_{\boldsymbol{x}}\boldsymbol{u}\nabla_{\boldsymbol{\xi}}\boldsymbol{x}$, and therefore $C(\zeta)$ in (3.1) satisfies:

$$\partial_\zeta C(\zeta) = \nabla_{\boldsymbol{\xi}}\boldsymbol{x}_\zeta^{\mathrm{T}}\nabla_{\boldsymbol{\xi}}\boldsymbol{x} + \nabla_{\boldsymbol{\xi}}\boldsymbol{x}^{\mathrm{T}}\nabla_{\boldsymbol{\xi}}\boldsymbol{x}_\zeta = \nabla_{\boldsymbol{\xi}}\boldsymbol{x}^{\mathrm{T}}\left[\nabla_{\boldsymbol{x}}\boldsymbol{u}^{\mathrm{T}} + \nabla_{\boldsymbol{x}}\boldsymbol{u}\right]\nabla_{\boldsymbol{\xi}}\boldsymbol{x}. \tag{3.5}$$

Hence, if $\nabla_{\boldsymbol{x}} \boldsymbol{u}$ is skew-symmetric, then $\partial_\zeta C(\zeta) = 0$ implies $C(\zeta) = C(0) = I$ and the transformation is rigid for all $\zeta \in [0, 1]$.

Now with (2.10) and (3.5), consider computing a registration by minimizing the following cost,

$$J_{\text{eul}}(I, \boldsymbol{u}) = \int_Q \left[(\nabla_{\boldsymbol{x}} I \cdot \boldsymbol{u} + I_z)^2 + \beta \left| \nabla_{\boldsymbol{x}} \boldsymbol{u}^{\mathrm{T}} + \nabla_{\boldsymbol{x}} \boldsymbol{u} \right|^2 \right] d\boldsymbol{x} dz \tag{3.6}$$

subject to $I = I_0$ on Ω_0, $I = I_1$ on Ω_1, and $I = 0$ on Γ. To test this formulation with $\hat{\boldsymbol{x}}$ and $\tilde{\boldsymbol{x}}$ as considered above, define $\hat{\boldsymbol{u}}(\boldsymbol{x}, z) = \hat{\boldsymbol{x}}_\zeta = W(\boldsymbol{x} - \boldsymbol{a})$ and $\tilde{\boldsymbol{u}}(\boldsymbol{x}, z) = \tilde{\boldsymbol{x}}_\zeta = [z + (R(1) - I)^{-1}]^{-1}(\boldsymbol{x} - \boldsymbol{a})$. As before, assume that the similarity term (2.10) is zero. Then an elementary calculation shows that $J_{\text{eul}}(\hat{\boldsymbol{u}}) = 0 < J_{\text{eul}}(\tilde{\boldsymbol{u}})$. In other words, the rigid-body motion is selected instead of the compression/expansion. It is also seen in the next section that the optimality system corresponding to (3.6) is computationally convenient.

4 Optimality Conditions

Image registration and interpolation are achieved in this work by minimizing the following cost,

$$J(I, \boldsymbol{u}) = \int_Q \left[(\nabla I \cdot \boldsymbol{u} + I_z)^2 + \phi \left(\left| \nabla \boldsymbol{u}^{\mathrm{T}} + \nabla \boldsymbol{u} \right|^2 \right) + \alpha \left| \boldsymbol{u}_z \right|^2 \right] d\boldsymbol{x} dz \tag{4.1}$$

subject to:

$$I = I_0 \ \text{ on } \ \Omega_0, \qquad I = I_1 \ \text{ on } \ \Omega_1, \qquad \text{and} \qquad I = 0 \ \text{ on } \ \Gamma. \tag{4.2}$$

Trajectories through the domain Q are defined by integrating the optical flow under boundary conditions, i.e., by solving:

$$\boldsymbol{x}(\boldsymbol{\xi}, \zeta) = \boldsymbol{\xi} + \int_0^\zeta \boldsymbol{u}(\boldsymbol{x}(\boldsymbol{\xi}, \rho), \rho) d\rho, \qquad \boldsymbol{\xi} \in \Omega_0, \quad \zeta \in [0, 1]. \tag{4.3}$$

and

$$\boldsymbol{y}(\boldsymbol{\eta}, \zeta) = \boldsymbol{\eta} + \int_\zeta^1 \boldsymbol{u}(\boldsymbol{y}(\boldsymbol{\eta}, \rho), \rho) d\rho, \qquad \boldsymbol{\eta} \in \Omega_1, \quad \zeta \in [0, 1]. \tag{4.4}$$

A registration is given by the coordinate transformation $\boldsymbol{x}(\boldsymbol{\xi}, 1)$ and by the inverse transformation $\boldsymbol{y}(\boldsymbol{\eta}, 0)$. The given images I_0 and I_1 are interpolated by the intensity I.

The function ϕ appearing in (4.1) is discussed further in Subsection 4.2, but it is assumed to be smooth on $(0, \infty)$ and continuous on $[0, \infty)$. Also, the term involving $\boldsymbol{u}_z$ is included to select the most natural rigid-body motion in Q as well as to establish the well-posedness shown below in Theorem 1.

With respect to the registration goal as stated in the Introduction, it may be observed now that the formulation in Q increases the problem dimenion by one. In this connection, the following points are worthwhile to emphasize. First, the present formulation affords image interpolation in addition to registration. Also, alternative diffusion processes evolving from Ω_0 to Ω_1 are here replaced by an elliptic formulation in Q with the payoff that the result is independent of the image order. Finally, these benefits are gained without an increased problem dimension if the optical flow is autonomous. Although the condition $\boldsymbol{u}_z = 0$ is not imposed explicitly in this work, it was found to hold practically in all examples presented in Section 6.

The necessary optimality conditions will now be derived first for I and then for $\boldsymbol{u}$. The intent is to solve cyclically for one variable with the other held fixed.

4.1 Optimality Conditions for Intensity

First, for fixed $\boldsymbol{u}$, the variational derivative of J with respect to I is given by

$$\frac{\delta J}{\delta I}(I; \bar{I}) = 2 \int_Q (\boldsymbol{\nabla} I \cdot \boldsymbol{w}) (\boldsymbol{\nabla} \bar{I} \cdot \boldsymbol{w}) \, d\boldsymbol{s} \tag{4.5}$$

where for convenience $\boldsymbol{\nabla} = (\nabla, \partial_z)$, $\boldsymbol{w} = (\boldsymbol{u}, 1)$, and $\boldsymbol{s} = (\boldsymbol{x}, z)$. Also, assume for the moment that I is only subject to $I = I_0$ on Ω_0 and $I = I_1$ on Ω_1, so that the perturbation $\bar{I}$ is constrained to vanish on Ω_0 and on Ω_1. Then, boundary integrals on Ω_0 and on Ω_1 vanish in the following:

$$\begin{aligned} \frac{\delta J}{\delta I}(I; \bar{I}) &= 2 \int_{\partial Q} (\boldsymbol{\nabla} I \cdot \boldsymbol{w})\, (\boldsymbol{w} \cdot \boldsymbol{\nu})\, \bar{I} d\boldsymbol{s} - 2 \int_Q \boldsymbol{\nabla} \cdot [(\boldsymbol{\nabla} I \cdot \boldsymbol{w})\, \boldsymbol{w}]\, \bar{I} d\boldsymbol{s} \\ &= 2 \int_\Gamma (\boldsymbol{\nabla} I \cdot \boldsymbol{w})\, (\boldsymbol{u} \cdot \boldsymbol{n})\, \bar{I} d\boldsymbol{s} - 2 \int_Q \boldsymbol{\nabla} \cdot [(\boldsymbol{\nabla} I \cdot \boldsymbol{w})\, \boldsymbol{w}]\, \bar{I} d\boldsymbol{s}. \end{aligned} \tag{4.6}$$

Here, $\boldsymbol{\nu}$ is an outwardly directed normal vector at ∂Q which reduces to $\boldsymbol{n}$ at Γ. For the variational derivative above to vanish for all perturbations $\bar{I}$, in particular for perturbations vanishing on the boundary Γ, the following equation must hold in the interior:

$$\begin{aligned} \boldsymbol{\nabla} \cdot [(\boldsymbol{\nabla} I \cdot \boldsymbol{w})\, \boldsymbol{w}] &= \nabla (\nabla I \cdot \boldsymbol{u} + I_z) \cdot \boldsymbol{u} + (\nabla I \cdot \boldsymbol{u} + I_z)_z + (\nabla \cdot \boldsymbol{u})\, (\nabla I \cdot \boldsymbol{u} + I_z) \\ &= \frac{d^2 I}{d\zeta^2} + (\nabla \cdot \boldsymbol{u}) \frac{dI}{d\zeta} = 0 \quad \text{in } Q \end{aligned} \tag{4.7}$$

in which (2.9) has been applied.

Consider now the choice of boundary conditions shown in (4.2). For the boundary term in (4.6) to vanish for all perturbations $\bar{I}$, there are three possibilities on Γ: $\bar{I} = 0$, $\boldsymbol{u} \cdot \boldsymbol{n} = 0$, or $\boldsymbol{\nabla} I \cdot \boldsymbol{w} = 0$. The first case corresponds to having imposed (4.2) so that the perturbation $\bar{I}$ would be constrained to vanish on all of ∂Q. To see the unsatisfactory consequences of the other two options, consider first that $\boldsymbol{u} \cdot \boldsymbol{n} = 0$ is imposed at Γ. This means that trajectories would not be allowed to impinge upon the boundary at Γ, and this restriction would clearly corrupt a rigid registration. Since it is required to produce a rigid registration when one fits the data, the boundary condition $\boldsymbol{u} \cdot \boldsymbol{n} = 0$ at Γ is ruled out. Now consider that $\boldsymbol{\nabla} I \cdot \boldsymbol{w} = dI/d\zeta = 0$ is imposed at Γ. Then fix a trajectory which departs from Ω_0 and impinges on Γ at $\zeta = \acute{\zeta}$ as shown in Fig. 2. From (4.7), the conditions on the trajectory that $d^2 I/d\zeta^2 + (\nabla \cdot \boldsymbol{u}) dI/d\zeta = 0$ for $0 < \zeta < \acute{\zeta}$, $I = I_0$ at $\zeta = 0$, and $dI/d\zeta = 0$ at $\zeta = \acute{\zeta}$ imply that I remains constant at $I = I_0$ along the trajectory. The situation is similar for trajectories that depart from Ω_1 and impinge upon Γ in the reverse direction. This is in fact a state toward which the solution $(I, \boldsymbol{u})$ would be drawn since it reduces the cost J. Specifically, when the intensity I is computed in this way, the optical flow $\boldsymbol{u}$ is drawn in its next iteration toward more trajectories that impinge upon Γ. Eventually all trajectories impinge upon Γ to give the minimum possible cost, and no like points in I_0 and I_1 are connected. Clearly, this is a solution to be avoided. Thus, the intensity field is assumed to satisfy the boundary conditions (4.2).

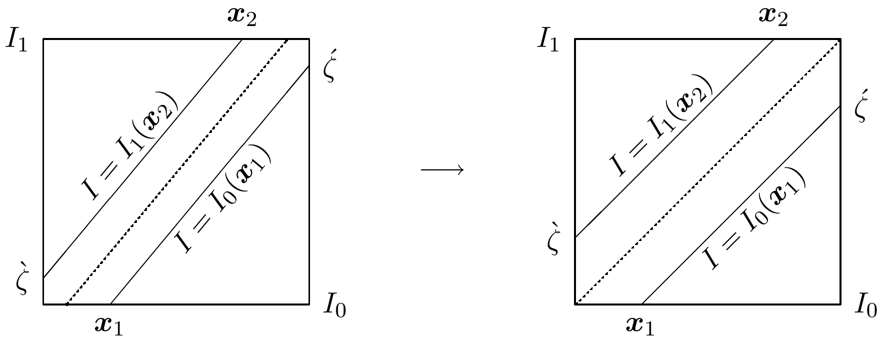

Figure 2: When the intensity I is constant along trajectories connected with Γ, all trajectories are drawn toward Γ until the cost J vanishes.

From (4.2) and (4.7), the optimal intensity I for fixed $\boldsymbol{u}$ is given in a Lagrangian frame by:

$$I(\boldsymbol{x}(\boldsymbol{\xi}, \zeta), \zeta) = \begin{cases} I_0(\boldsymbol{\xi})[1 - U(\boldsymbol{\xi}, \zeta, 1)] + I_1(\boldsymbol{x}(\boldsymbol{\xi}, 1)) U(\boldsymbol{\xi}, \zeta, 1), & \boldsymbol{\xi} \in \Omega_0^{\mathrm{c}} \\ I_0(\boldsymbol{\xi})[1 - U(\boldsymbol{\xi}, \zeta, \acute{\zeta})], \qquad \boldsymbol{x}(\boldsymbol{\xi}, \acute{\zeta}) \in \Gamma, & \boldsymbol{\xi} \in \Omega_0^{\mathrm{i}} \\ I_0(\boldsymbol{\xi}), \qquad \boldsymbol{x}(\boldsymbol{\xi}, \acute{\zeta}) \in \Xi, & \boldsymbol{\xi} \in \Omega_0^{\mathrm{i}}, \end{cases} \tag{4.8}$$

and:

$$I(\boldsymbol{y}(\boldsymbol{\eta},\zeta),\zeta) = \begin{cases} I_1(\boldsymbol{\eta})[1-V(\boldsymbol{\eta},0,\zeta)] + I_0(\boldsymbol{y}(\boldsymbol{\eta},0))V(\boldsymbol{\eta},0,\zeta), & \boldsymbol{\eta}\in\Omega_1^{\mathrm{c}} \\ I_1(\boldsymbol{\eta})[1-V(\boldsymbol{\eta},\grave{\zeta},\zeta)], \qquad \boldsymbol{y}(\boldsymbol{\eta},\grave{\zeta})\in\Gamma, & \boldsymbol{\eta}\in\Omega_1^{\mathrm{i}} \\ I_1(\boldsymbol{\eta}), \qquad \boldsymbol{y}(\boldsymbol{\eta},\grave{\zeta})\in\Xi, & \boldsymbol{\eta}\in\Omega_1^{\mathrm{i}} \end{cases} \tag{4.9}$$

in terms of quantities defined as follows. Here, Ω_0^{c} and Ω_0^{i} are the disjoint subsets of Ω_0 from which trajectories extend completely and incompletely, respectively, through the full depth of Q. Also, Ω_1^{c} and Ω_1^{i} are disjoint subsets of Ω_1 defined similarly. Let $\Xi \subset Q$ denote a set in which trajectories fail to be well defined, e.g., due to a singularity in the optical flow field. Define U and V by:

$$U(\boldsymbol{\xi},\zeta,\acute{\zeta}) = \begin{cases} \dfrac{\tilde{U}(\boldsymbol{\xi},\zeta)-\tilde{U}(\boldsymbol{\xi},0)}{\tilde{U}(\boldsymbol{\xi},\acute{\zeta})-\tilde{U}(\boldsymbol{\xi},0)}, \\ \\ 0, \quad \boldsymbol{x}(\boldsymbol{\xi},\acute{\zeta})\in\Xi, \end{cases} \qquad \tilde{U}(\boldsymbol{\xi},\zeta) = \int_{\zeta_0}^{\zeta} \exp\left[-\int_{\zeta_0}^{\sigma} \nabla\cdot\boldsymbol{u}(\boldsymbol{x}(\boldsymbol{\xi},\rho),\rho)d\rho\right] d\sigma, \tag{4.10}$$

for $\boldsymbol{\xi}\in\Omega_0$, $\zeta\in[0,\acute{\zeta}]$, and arbitrary $\zeta_0\in[0,\acute{\zeta}]$, and:

$$V(\boldsymbol{\eta},\grave{\zeta},\zeta) = \begin{cases} \dfrac{\tilde{V}(\boldsymbol{\eta},1)-\tilde{V}(\boldsymbol{\eta},\zeta)}{\tilde{V}(\boldsymbol{\eta},1)-\tilde{V}(\boldsymbol{\eta},\grave{\zeta})}, \\ \\ 0, \quad \boldsymbol{y}(\boldsymbol{\eta},\grave{\zeta})\in\Xi, \end{cases} \qquad \tilde{V}(\boldsymbol{\eta},\zeta) = \int_{\zeta_0}^{\zeta} \exp\left[-\int_{\zeta_0}^{\sigma} \nabla\cdot\boldsymbol{u}(\boldsymbol{y}(\boldsymbol{\eta},\rho),\rho)d\rho\right] d\sigma, \tag{4.11}$$

for $\boldsymbol{\eta}\in\Omega_1$, $\zeta\in[\grave{\zeta},1]$, and arbitrary $\zeta_0\in[\grave{\zeta},1]$. Under a condition such as $\boldsymbol{u}\in W^{1,\infty}(Q)\subset C^{0,1}(\bar{Q})$ [30], trajectories are well defined by (4.3) and (4.4) and the singular set Ξ is empty [8]. On the other hand, it is not intended to rule out situations where the registration is correctly described by a discontinuous optical flow field which would occur for instance when an object is excised. Suppose that $\Xi\subset Q$ denotes the set where shocks develop in the optical flow field as seen below in Fig. 3. Then trajectories are defined up to the shock and the intensity is constant along such trajectories as shown in (4.8) and (4.9). At all other points in Q not accessible from trajectories (4.3) or (4.4) the intensity is zero.

4.2 Optimality Conditions for Optical Flow

Now, for fixed I, the variational derivative of J with respect to $\boldsymbol{u}$ is given by

$$\begin{aligned} \frac{\delta J}{\delta \boldsymbol{u}}(\boldsymbol{u};\bar{\boldsymbol{u}}) &= 2\int_Q \left[(\nabla I\cdot\boldsymbol{u}+I_z)(\nabla I\cdot\bar{\boldsymbol{u}}) + \alpha\,(\boldsymbol{u}_z\cdot\bar{\boldsymbol{u}}_z)\right] d\boldsymbol{x}dz \\ &+ 2\int_Q \phi'\left(\left|\nabla\boldsymbol{u}^{\mathrm{T}}+\nabla\boldsymbol{u}\right|^2\right)\left[\nabla\boldsymbol{u}^{\mathrm{T}}+\nabla\boldsymbol{u}\right]:\left[\nabla\bar{\boldsymbol{u}}^{\mathrm{T}}+\nabla\bar{\boldsymbol{u}}\right] d\boldsymbol{x}dz. \end{aligned} \tag{4.12}$$

The optical flow $\boldsymbol{u}$ is computed by solving the weakly formulated optimality system,

$$0 = \frac{1}{2}\frac{\delta J}{\delta\boldsymbol{u}}(\boldsymbol{u};\bar{\boldsymbol{u}}) = B(\boldsymbol{u},\boldsymbol{u},\bar{\boldsymbol{u}}) - F(\bar{\boldsymbol{u}}), \qquad \forall\bar{\boldsymbol{u}}\in C^{\infty}(\bar{Q}), \tag{4.13}$$

where B and F are defined as follows:

$$\begin{aligned} B(\boldsymbol{u},\boldsymbol{v},\boldsymbol{w}) &= \int_Q \left[(\nabla I\cdot\boldsymbol{v})(\nabla I\cdot\boldsymbol{w}) + \alpha\,(\boldsymbol{v}_z\cdot\boldsymbol{w}_z)\right] d\boldsymbol{x}dz \\ &+ \int_Q \phi'\left(\left|\nabla\boldsymbol{u}^{\mathrm{T}}+\nabla\boldsymbol{u}\right|^2\right)\left(\nabla\boldsymbol{v}^{\mathrm{T}}+\nabla\boldsymbol{v}\right):\left(\nabla\boldsymbol{w}^{\mathrm{T}}+\nabla\boldsymbol{w}\right) d\boldsymbol{x}dz \end{aligned} \tag{4.14}$$

$$F(\boldsymbol{w}) = -\int_Q I_z\nabla I\cdot\boldsymbol{w}d\boldsymbol{x}dz. \tag{4.15}$$

The solvability of (4.13) is considered below in Theorem 1 for linear ϕ. The optimality system is also given below in differential form. As explained in connection with (4.6), only natural boundary conditions are considered for $\boldsymbol{u}$ in order to avoid disturbances to rigid registrations, and therefore, the above variational derivative satisfies

$$\begin{aligned}\frac{1}{2}\frac{\delta J}{\delta \boldsymbol{u}}(\boldsymbol{u};\bar{\boldsymbol{u}}) = &\int_Q \left\{(\nabla I\cdot\boldsymbol{u}+I_z)\nabla I-\alpha\boldsymbol{u}_{zz}-\nabla\cdot\left[2\phi'\left(\left|\nabla\boldsymbol{u}^{\mathrm{T}}+\nabla\boldsymbol{u}\right|^2\right)\left(\nabla\boldsymbol{u}^{\mathrm{T}}+\nabla\boldsymbol{u}\right)\right]\right\}\cdot\bar{\boldsymbol{u}}d\boldsymbol{x}dz\\ &+\int_\Gamma \boldsymbol{n}\cdot\left[2\phi'\left(\left|\nabla\boldsymbol{u}^{\mathrm{T}}+\nabla\boldsymbol{u}\right|^2\right)\left(\nabla\boldsymbol{u}^{\mathrm{T}}+\nabla\boldsymbol{u}\right)\right]\cdot\bar{\boldsymbol{u}}d\boldsymbol{x}dz+\int_{\Omega_1}\alpha\boldsymbol{u}_z\cdot\bar{\boldsymbol{u}}d\boldsymbol{x}-\int_{\Omega_0}\alpha\boldsymbol{u}_z\cdot\bar{\boldsymbol{u}}d\boldsymbol{x}.\end{aligned} \tag{4.16}$$

Requiring this variational derivative to vanish for smooth perturbations $\bar{\boldsymbol{u}}$ which have vanishingly small support while remaining concentrated at a given point in a single integral above leads to the following optimality conditions on the optical flow $\boldsymbol{u}$:

$$\left\{\begin{array}{l} -2\nabla\cdot\left[\phi'\left(\left|\nabla\boldsymbol{u}^{\mathrm{T}}+\nabla\boldsymbol{u}\right|^2\right)\left(\nabla\boldsymbol{u}^{\mathrm{T}}+\nabla\boldsymbol{u}\right)\right]-\alpha\boldsymbol{u}_{zz}+\left(\nabla I\nabla I^{\mathrm{T}}\right)\boldsymbol{u}=-I_z\nabla I,\quad Q,\\[2ex] \qquad\qquad \boldsymbol{n}\cdot\left(\nabla\boldsymbol{u}^{\mathrm{T}}+\nabla\boldsymbol{u}\right)=0,\quad \Gamma,\qquad\qquad \boldsymbol{u}_z=0,\quad \Omega_0,\ \Omega_1.\end{array}\right. \tag{4.17}$$

To illustrate the effect of the function ϕ, consider the system for one-dimensional images, $I_{\mathrm{e}}(x,0)$ and $I_{\mathrm{e}}(x,1)$ from $I_{\mathrm{e}}(x,z)=\max\{(1-\frac{1}{2}z)-2|x-\frac{1}{2}|,0\}$, which model the excision of an object $\{I_{\mathrm{e}}(x,0)>\frac{1}{2}\}$ in Ω_0 as shown in Fig. 3. The natural corresponding optical flow is $u_{\mathrm{e}}(x,z)=\frac{1}{4}\chi_{[0,1/2]}(x)-\frac{1}{4}\chi_{[1/2,1]}(x)$, but the corresponding cost is not finite if ϕ is linear. Instead, the fitting penalty in this case is total variation $\phi(s)=\beta\sqrt{s}$,

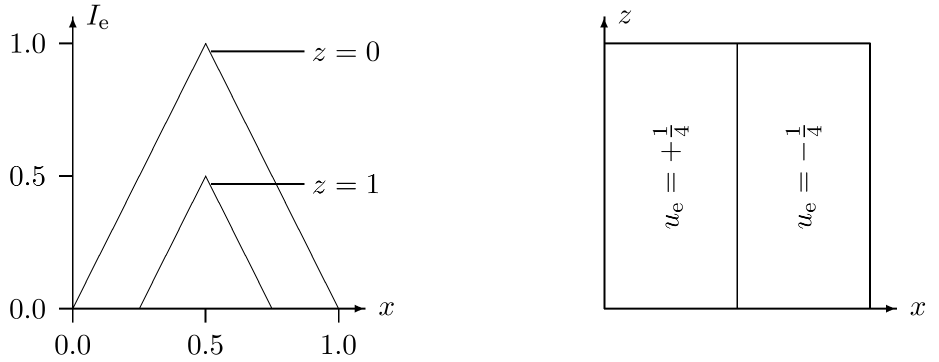

Figure 3: The intensity I_{e} models the excision of an object from Ω_0, and the discontinuous u_{e} is the natural corresponding optical flow.

$$J(u)=\int_0^1\int_{\frac{z}{4}}^{\frac{1}{2}}(2u-\tfrac{1}{2})^2dxdz+\int_0^1\int_{\frac{1}{2}}^{1-\frac{z}{4}}(2u+\tfrac{1}{2})^2dxdz+\int_0^1\int_0^1\left[2\beta|u_x|+\alpha|u_z|^2\right]dxdz \tag{4.18}$$

for which $J(u_{\mathrm{e}})=\beta$ and for which (4.13) holds with $u=u_{\mathrm{e}}$. Note the difficulty in implementing such singular transformations in a purely Lagrangian frame such as with (3.4). Of course, if smoother registrations are desired, then choosing a linear function ϕ is more appropriate. Intermediate regularization goals can be reached through intermediate choices for ϕ [33], but it is assumed here that $\phi(s^2)$ is convex for well-posed minimization [3].

4.3 Well-Posedness of the Variational Problem

It is not quite clear beforehand whether the cost function (4.1) is sufficiently coercive with respect to $\boldsymbol{u}$ to quarantee well-posedness for (4.13) or whether additional optical flow regularization such as

$$\int_Q\phi\left(|\nabla\boldsymbol{u}|^2\right)d\boldsymbol{x}dz \tag{4.19}$$

is necessary. For instance, suppose the intensity has the form $I(\boldsymbol{x}, z) = |\boldsymbol{x}|^2$ in Q, and thereby supports an ambiguous optical flow $\boldsymbol{u}_\theta = \theta W \boldsymbol{x}$ for any $\theta \in \boldsymbol{R}$ and for any skew-symmetric matrix $W \in \boldsymbol{R}^{N \times N}$. Then the cost is zero for every $\theta \in \boldsymbol{R}$, and in particular $J(\boldsymbol{u}_\theta) \not\to \infty$ as $\|\boldsymbol{u}_\theta\|_{H^1(Q)} = \mathcal{O}(\theta) \to \infty$. However, it can be assumed safely that medical images do not support such ambiguity. Thus, on the basis of the following theorem, the regularization shown in (4.19) is not used in this work.

Theorem 1 *Suppose that an intensity* $I \in W^{1,\infty}(Q)$ *manifests sufficiently few symmetries that for every* $\boldsymbol{a} \in \boldsymbol{R}^N$ *and for every skew-symmetric* $W \in \boldsymbol{R}^{N \times N}$*,*

$$\int_Q |\nabla I \cdot (\boldsymbol{a} + W\boldsymbol{x})|^2 d\boldsymbol{x} dz > 0, \tag{4.20}$$

unless $\boldsymbol{a} = 0 = W$*. Then with* $\phi(s) = \beta(\boldsymbol{x}, z)s$*,* $0 < \beta_0 \leq \beta(\boldsymbol{x}, z) \leq \beta_1 < \infty$*, there exists a unique* $\boldsymbol{u} \in H^1(Q)$ *such that (4.13) holds.*

Proof: Since $C^\infty(\bar{Q})$ is dense in $H^1(Q)$, the claim follows from the Lax-Milgram Lemma [5] once it is shown that $B(\boldsymbol{u}, \boldsymbol{v}) = B(\cdot, \boldsymbol{u}, \boldsymbol{v})$ is bounded and coercive on $H^1(Q)$ and that $F(\boldsymbol{v})$ is bounded on $H^1(Q)$. The boundedness of B and F is readily established:

$$\begin{aligned} |B(\boldsymbol{u}, \boldsymbol{v})| &\leq \|I\|^2_{W^{1,\infty}(Q)} \|\boldsymbol{u}\|_{L^2(Q)} \|\boldsymbol{v}\|_{L^2(Q)} + \alpha \|\boldsymbol{u}_z\|_{L^2(Q)} \|\boldsymbol{v}_z\|_{L^2(Q)} + 4\beta_1 \|\nabla \boldsymbol{u}\|_{L^2(Q)} \|\nabla \boldsymbol{v}\|_{L^2(Q)} \\ &\leq [\|I\|^2_{W^{1,\infty}(Q)} + \alpha + 4\beta_1] \|\boldsymbol{u}\|_{H^1(Q)} \|\boldsymbol{v}\|_{H^1(Q)} \qquad (4.21) \\ |F(\boldsymbol{v})| &\leq \|I\|^2_{W^{1,\infty}(Q)} \|\boldsymbol{v}\|_{L^2(Q)}. \qquad (4.22) \end{aligned}$$

To establish coercivity of B, assume there exists a sequence $\{\boldsymbol{u}_n\} \subset H^1(Q)$ such that

$$\|\boldsymbol{u}_n\|_{H^1(Q)} = 1 \qquad \text{while} \qquad B(\boldsymbol{u}_n, \boldsymbol{u}_n) \to 0. \tag{4.23}$$

For convenience, define now the semi-norm $|\cdot|_B$ satisfying the following inequality:

$$|\boldsymbol{u}|_B^2 = \|\nabla \boldsymbol{u}^{\mathrm{T}} + \nabla \boldsymbol{u}\|^2_{L^2(Q)} + \|\boldsymbol{u}_z\|^2_{L^2(Q)} \leq \frac{1}{\min\{\alpha, \beta_0\}} B(\boldsymbol{u}, \boldsymbol{u}). \tag{4.24}$$

Since $H^1(Q)$ is compactly embedded in $L^2(Q)$ [1], there is a subsequence $\{\boldsymbol{u}_{n_l}\}$ which converges in $L^2(Q)$. From Korn's Inequality [27],

$$\|\nabla \boldsymbol{u}\|^2_{L^2(Q)} \leq k_1 \|\boldsymbol{u}\|^2_{L^2(Q)} + k_2 \|\nabla \boldsymbol{u}^{\mathrm{T}} + \nabla \boldsymbol{u}\|^2_{L^2(Q)} \tag{4.25}$$

it follows that

$$\|\boldsymbol{u}_{n_l} - \boldsymbol{u}_{n_k}\|_{H^1(Q)} \leq c_1 \|\boldsymbol{u}_{n_l} - \boldsymbol{u}_{n_k}\|_{L^2(Q)} + c_2 |\boldsymbol{u}_{n_l} - \boldsymbol{u}_{n_k}|_B. \tag{4.26}$$

Since both terms on the right vanish, it follows that $\{\boldsymbol{u}_{n_l}\}$ is a Cauchy sequence in $H^1(Q)$ with some limit $\boldsymbol{u}^* \in H^1(Q)$ which satisfies:

$$\min\{\alpha, \beta_0\} |\boldsymbol{u}^*|_B^2 \leq B(\boldsymbol{u}^*, \boldsymbol{u}^*) = \lim_{n_l \to 0} B(\boldsymbol{u}_{n_l}, \boldsymbol{u}_{n_l}) = 0. \tag{4.27}$$

From (4.24) and (4.27) it follows that $\partial_z u_i^* = 0 = e_{ij}^* = \frac{1}{2}(\partial_{x_i} u_j^* + \partial_{x_j} u_i^*)$. Thus, $\boldsymbol{u}^*$ is independent of z. From the identity $\partial_{x_i x_j} u_k^* = \partial_{x_i} e_{jk}^* + \partial_{x_j} e_{ki}^* - \partial_{x_k} e_{ij}^*$ [7], it follows that $\boldsymbol{u}^*$ is a linear function of $\boldsymbol{x}$. Since $e_{ij}^* = 0$, $\boldsymbol{u}^*$ is given by $\boldsymbol{u}^* = \boldsymbol{a} + W\boldsymbol{x}$ for some $\boldsymbol{a} \in \boldsymbol{R}^N$ and some skew-symmetric $W \in \boldsymbol{R}^{N \times N}$. Then from $B(\boldsymbol{u}^*, \boldsymbol{u}^*) = 0$ it follows that the integral in (4.20) vanishes. However, this violates the assumption on I unless $\boldsymbol{u}^* = 0$, which contradicts the assumption that $\|\boldsymbol{u}_n\|_{H^1(Q)} = 1$. Thus, B is coercive on $H^1(Q)$. ■

Although details are not provided here, it is assumed that if $I \in W^{1,\infty}(Q)$ then $\boldsymbol{u} \in W^{1,\infty}(Q)$ [30], as mentioned in Subsection 4.1 concerning conditions under which trajectories are globally well-defined. When the given images are so noisy that only $I_0 \in BV(\Omega_0)$ and $I_1 \in BV(\Omega_1)$ can be assumed, then additional intensity regularization can be considered, similar to that found in [2]. Otherwise, global existence of trajectories can be assured by representing I_0 and I_1 in terms of their multilinear interpolants.

5 Numerical Approximation

The discretizations of (4.7) and (4.17) are described separately in the subsections below with the intent to implement them in the following loop by solving for one variable while the other is held fixed:

- Set $\boldsymbol{u} = 0$.
- Repeat until the relative difference in $\boldsymbol{u}$ is sufficiently small:
  - Compute I from $\boldsymbol{u}$ as specified in Subsection 5.1.
  - Compute $\boldsymbol{u}$ from I as specified in Subsection 5.2.

While the convergence of this cycling is not proved here, convergence has been observed for all examples presented in Section 6.

The numerical discretization begins with a division of Q into a grid of cells, each having dimensions $(h, \dots, h, \tau)$, in the $x_1, \dots, x_N$, and z directions, respectively, where $h = 2^{-p}$ and $\tau = 1/K$ for integers p and K. Specifically, with the integer-component N-dimensional multi-indices $\boldsymbol{i} = (i_1, \dots, i_N)$, $\mathbf{0} = (0, \dots, 0)$, and $\mathbf{1} = (1, \dots, 1)$, define the cell corners by $(\mathrm{x}_{\boldsymbol{i}+1/2}, \mathrm{z}_{k+1/2}) = (\boldsymbol{i}h, k\tau)$, $\mathbf{0} \le \boldsymbol{i} \le 2^p \cdot \mathbf{1}$, $0 \le k \le K$, and the cell centroids by $(\mathrm{x}_{\boldsymbol{i}}, \mathrm{z}_k) = ((\boldsymbol{i} - \frac{\mathbf{1}}{2})h, (k - \frac{1}{2})\tau)$, $\mathbf{1} \le \boldsymbol{i} \le 2^p \cdot \mathbf{1}$, $1 \le k \le K$. Then, the notation $f_{\boldsymbol{i},k}$ is used for a grid function at the cell centroid $(\boldsymbol{i}, k)$, and fractional indices are used for cell boundaries. The given images I_0 and I_1 are imposed numerically as boundary conditions, $I_{\boldsymbol{i},k_0} = I_{0,\boldsymbol{i}}$ and $I_{\boldsymbol{i},k_1} = I_{1,\boldsymbol{i}}$ in the cell face coordinates $(\boldsymbol{i}, k_0)$ and $(\boldsymbol{i}, k_1)$, respectively, where $k_0 = \frac{1}{2}$ and $k_1 = K + \frac{1}{2}$.

5.1 Intensity Discretization

To discuss the effects of different discretizations, the following model situation is considered. Suppose with $\boldsymbol{x}(\boldsymbol{\xi}, \zeta) = \boldsymbol{\xi} + \boldsymbol{u}\zeta$ and $\boldsymbol{u} = (1/\sqrt{2}, 1/\sqrt{2})$, that the given images are related by a simple translation, $I_0(\boldsymbol{\xi}) = I_1(\boldsymbol{\xi} + \boldsymbol{u})$. Thus, $\nabla \cdot \boldsymbol{u} = 0$ and (4.7) takes the form,

$$\nabla\left(\nabla I \cdot \boldsymbol{u} + I_z\right) \cdot \boldsymbol{u} + \left(\nabla I \cdot \boldsymbol{u} + I_z\right)_z = \frac{d^2 I}{d\zeta^2} = 0. \tag{5.1}$$

Assume that the intensity is represented as a grid function $I_{\boldsymbol{i},k}$. Then, an Eulerian discretization of (5.1) takes the form,

$$I_{(\boldsymbol{i}+\boldsymbol{u}\tau/h,k+1)} - 2I_{\boldsymbol{i},k} + I_{(\boldsymbol{i}-\boldsymbol{u}\tau/h,k-1)} = 0 \tag{5.2}$$

solved for example through iteration by

$$I^{\ell}_{\boldsymbol{i},k} = \frac{1}{2}\left[I^{\ell-1}_{(\boldsymbol{i}+\boldsymbol{u}\tau/h,k+1)} + I^{\ell-1}_{(\boldsymbol{i}-\boldsymbol{u}\tau/h,k-1)}\right] \tag{5.3}$$

where the values $I_{(\boldsymbol{i}+\boldsymbol{u}\tau/h,k+1)}$ and $I_{(\boldsymbol{i}-\boldsymbol{u}\tau/h,k-1)}$ must be interpolated from nearby intensity grid values. To see the consequences of such an interpolation, consider the case illustrated in Fig. 4 where $I_0(\boldsymbol{x}) = \chi_S(\boldsymbol{x})$ and $I_1(\boldsymbol{x}) = \chi_S(\boldsymbol{x} - \boldsymbol{u})$ for the square $S = \{\boldsymbol{x} : 0 \le x_1, x_2 \le \frac{1}{2}\}$, and the correct intensity I is defined on Q as equal to one in the diagonal zone and zero otherwise. Let

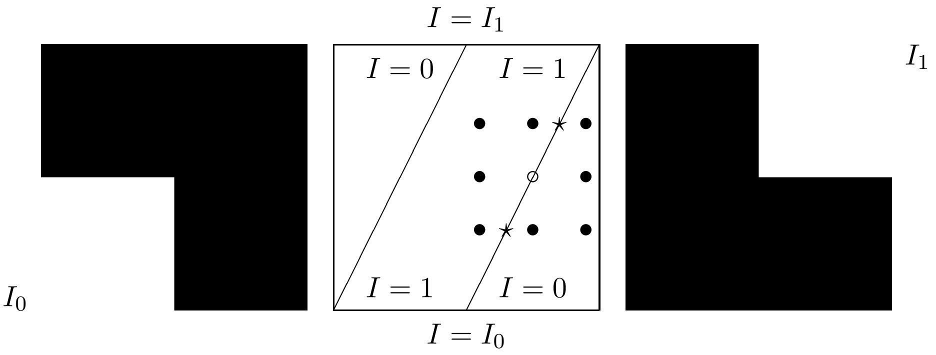

Figure 4: The given images I_0 and I_1 are shown on the left and on the right, respectively, and a planview of the correct intensity I in Q is illustrated in the middle, along with an Eulerian discretization around the empty circle.

the empty circle denote the cell $(\boldsymbol{i}, k)$, the filled circles its cell neighbors, and the stars the cell coordinates $(\boldsymbol{i} \pm \boldsymbol{u}\tau/h, k \pm 1)$. Then, a natural linear interpolation of intensity grid values in the respective neighborhoods gives $I_{(\boldsymbol{i}+\boldsymbol{u}\tau/h,k+1)} = \frac{1}{2} = I_{(\boldsymbol{i}-\boldsymbol{u}\tau/h,k-1)}$, and therefore from (5.3) the value of $I_{\boldsymbol{i},k}$ drops from one to one-half. Repeated application of (5.3) produces the results shown in Fig. 5, where for the given 32×32 images I_0 and I_1 shown in Fig. 4, intermediate images

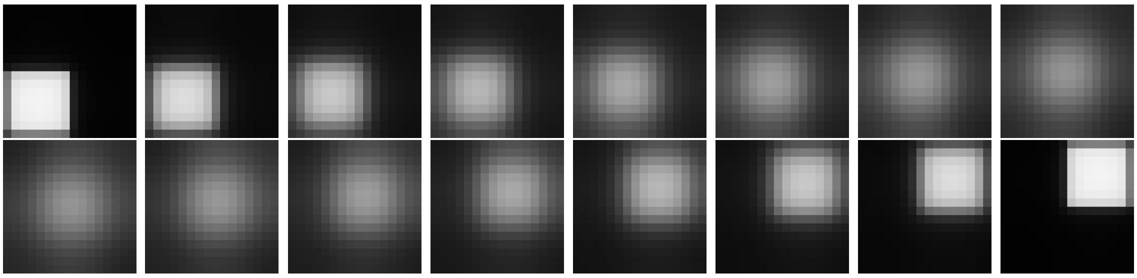

Figure 5: For the given 32×32 images I_0 and I_1 shown in Fig. 4, intermediate images $\{\{I_{\boldsymbol{i},k}\} : 1 \leq k \leq 16\}$ computed with an Eulerian discretization of (5.1) are read from left to right and from top to bottom.

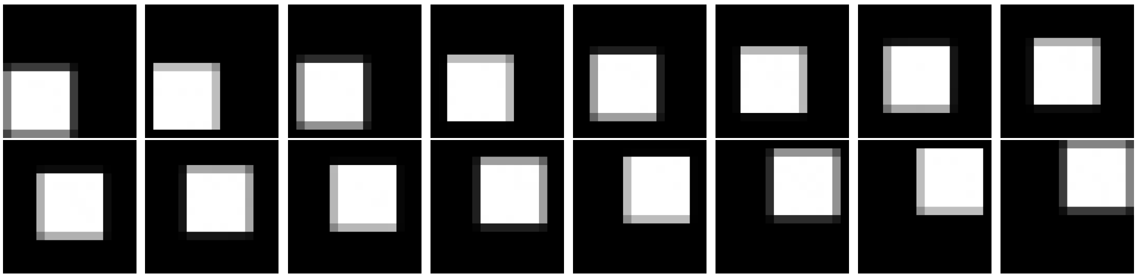

Figure 6: For the given 32×32 images I_0 and I_1 shown in Fig. 4, intermediate images $\{\{I_{\boldsymbol{i},k}\} : 1 \leq k \leq 16\}$ computed with a Lagrangian discretization of (5.1) are read from left to right and from top to bottom.

$\{\{I_{\boldsymbol{i},k}\} : 1 \leq k \leq 16\}$, are read in Fig. 5 from left to right and from top to bottom. Clearly, the linear interpolation is too dissipative, and although nonlinear interpolation operators can be considered, the conclusion from this experiment was that a Lagrangian discretization of (4.7) is preferred over an Eulerian one. In fact, the results shown in Fig. 6 reflect the improvement obtained from the Eulerian discretization described below.

The discretization of (4.8) and (4.9) requires first an integration through the optical flow field $\boldsymbol{u}$ in (4.3) and (4.4) to obtain trajectories $\boldsymbol{x}(\boldsymbol{\xi}, \zeta)$ and $\boldsymbol{y}(\boldsymbol{\eta}, \zeta)$ impinging on Ω_0 and on Ω_1 as illustrated in Fig. 2. The intensity discretization requires secondly an integration through the divergence field $\nabla \cdot \boldsymbol{u}$ in (4.10) and (4.11) to obtain $U(\boldsymbol{\xi}, \zeta, \acute{\zeta})$ and $V(\boldsymbol{\eta}, \grave{\zeta}, \zeta)$ for (4.8) and (4.9). However, the optical flow discretization remains Eulerian. Therefore, multilinear interpolation of the values $\{\boldsymbol{u}_{\boldsymbol{i},k}\}$ is used to represent $\boldsymbol{u}$ for (4.3) and (4.4). Similarly, multilinear interpolation of the values $\{\nabla_h \cdot \boldsymbol{u}_{\boldsymbol{i},k}\}$ is used to represent the divergence $\nabla \cdot \boldsymbol{u}$ in (4.10) and (4.11), where $\nabla_h \cdot \boldsymbol{u}_{\boldsymbol{i},k}$ is obtained by central differences with natural one-sided modifications at the boundary. Outside the convex hull of centroids, $\boldsymbol{u}$ and $\nabla \cdot \boldsymbol{u}$ are represented by multilinear extrapolation. With the interpolated optical flow vector and divergence fields, the integrals in (4.3), (4.4), (4.10), and (4.11) are approximated using a Runge-Kutta-Fehlberg adaptive integration.

Although the discretization chosen for (4.7) is Lagrangian, intensity grid values are needed for the Eulerian discretization of (4.17). In order to perform image morphing, intensity values are also needed along trajectories emanating from front cell faces $\{(\boldsymbol{i}, k_0)\}$ and from rear cell faces $\{(\boldsymbol{i}, k_1)\}$. Therefore, one option is to calculate only those trajectories emanating from front or rear cell faces, to solve for the intensity along these trajectories, and then to interpolate these intensity values onto interior cells to obtain intensity grid values for (4.17). However, such interpolation leads again to smoothing problems as illustrated in Figs. 4 and 5. Thus, the chosen procedure is to generate trajectories emanating from every cell centroid $(\mathrm{x}_{\boldsymbol{i}}, \mathrm{z}_k)$, both toward Ω_0 and toward Ω_1 so that with (4.8) and (4.9) an intensity grid function can be obtained without interpolation. For this, ζ_0 in (4.10) and (4.11) is set to its value at a cell centroid. In spite of the apparent expense of these integrations, note that they are independent, but require individual treatment to halt integration once the boundary Γ or an irregular flow zone Ξ has been reached. Nevertheless, the integrations can be vectorized by maintaining a grid function,

$$\varpi_{\boldsymbol{i},k} = \begin{cases} 1, & \text{trajectory through } (\mathrm{x}_{\boldsymbol{i}}, \mathrm{z}_k) \text{ advances through } Q, \\ 0, & \text{otherwise} \end{cases} \tag{5.4}$$

which always multiplies trajectory increments and which switches from one to zero after a trajectory has reached Γ or Ξ. While it is clear when the boundary Γ has been reached, an arrival criterion for the set Ξ can be implemented numerically in terms of whether an integration accuracy criterion has been met. Once a trajectory reaches the boundary of Q, the intensity I is computed from (4.8) and (4.9) using multilinear interpolation from face centroid values of I_0 on Ω_0 and I_1 on Ω_1 and from $I = 0$ on Γ.

The computation of the intensity can now be summarized as follows:

- From each cell centroid, integrate (4.3) and (4.4) to generate trajectories $\boldsymbol{x}$ and $\boldsymbol{y}$ directed toward Ω_0 and Ω_1, respectively.
- Simultaneously integrate (4.10) and (4.11) to obtain U and V.
- While integrating, represent $\boldsymbol{u}$ and $\nabla \cdot \boldsymbol{u}$ by multilinear interpolation and extrapolation from cell centroids.
- Represent the intensity on the boundary of Q by multilinear interpolation from face centroid values of I_0 on Ω_0 and I_1 on Ω_1 and from $I = 0$ on Γ.
- Compute the intensity I at each cell centroid using in (4.8) and (4.9).

5.2 Optical Flow Discretization

Now, consider the computation of the optical flow $\boldsymbol{u}$ from (4.17). The numerical approximation is obtained naturally from a finite element discretization of (4.12) [5]. Specifically, let $S_{h,\tau}$ be the space of tensor products of linear C^0 splines defined on Q, and let $\boldsymbol{u} \in S_{h,\tau}$ be determined by:

$$B(\boldsymbol{u}, \boldsymbol{u}, \boldsymbol{\chi}) = F(\boldsymbol{\chi}), \qquad \forall \boldsymbol{\chi} \in S_{h,\tau} \tag{5.5}$$

where B and F are given in (4.14) and (4.15). Because of the possible nonlinearity, ϕ' in (5.5), a lagged diffusivity iteration is used [32]. Specifically, given $\boldsymbol{u}^{\ell-1} \in S_{h,\tau}$, let $\boldsymbol{u}^{\ell} \in S_{h,\tau}$ be determined by:

$$B(\boldsymbol{u}^{\ell-1}, \boldsymbol{u}^{\ell}, \boldsymbol{\chi}) = F(\boldsymbol{\chi}), \qquad \forall \boldsymbol{\chi} \in S_{h,\tau}. \tag{5.6}$$

For this, assume that ϕ is sufficiently regularized so that $0 < \beta_0 \le \phi' \le \beta_1 < \infty$. Thus, by Theorem 1, $\boldsymbol{u}^{\ell}$ is well-defined by (5.6).

As illustrated in [17], finite element discretizations lead to aberrant consequences in the limit of vanishing regularization corresponding to an ever improving signal-to-noise ratio. To avoid these consequences as well as the wide bandwidth of the algebraic system in (5.6), a *lumping* approach is used to derive a finite difference discretization which is consistent with (5.6). Such lumping is implemented here by using cell-centered tensor products of spline basis functions:

$$s^{(0)}(t) = \chi_{[0,1]}(t), \quad s^{(1)}(t) = [s^{(0)} * s^{(0)}](t)$$

$$\begin{array}{rccl} s^{(m_i)}(h^{-1}x_i - \boldsymbol{N} + \frac{m_i}{2}) & \text{on} & Q_{x_i} & = & [\frac{m_i}{2}h, 1 - \frac{m_i}{2}h] \\ s^{(n)}(\tau^{-1}z - \boldsymbol{N} + \frac{n}{2}) & \text{on} & Q_z & = & [\frac{n}{2}\tau, 1 - \frac{n}{2}\tau]. \end{array} \tag{5.7}$$

$$Q \approx \hat{Q} = Q_{x_1} \times \cdots \times Q_{x_N} \times Q_z$$

which are minimally smooth in a given direction for a given term as detailed below. The effect of this lumping is to concentrate the algebraic formulation at cell centers. Thus, the final system unknowns become the optical flow grid values directly instead of merely finite element basis function weights.

Lumping is implemented for the term $\int_{\hat{Q}} (\nabla I \cdot \boldsymbol{u})(\nabla I \cdot \boldsymbol{\chi}) d\boldsymbol{x}dz$ from $B(\boldsymbol{u}^{\ell-1}, \boldsymbol{u}, \boldsymbol{\chi})$ with $m_i = n = 0$ in (5.7) and leads to the algebraic coefficients $(\nabla I_{\boldsymbol{i},k} \nabla I^{\mathrm{T}}_{\boldsymbol{i},k})\boldsymbol{u}_{\boldsymbol{i},k}$. Here, the numerical gradient $\nabla_h I$ is computed with simple central differences with natural one-sided modifications at the boundary. In spite of the apparent wavelike nature of the transport of intensities through Q, nonlinear gradient approximations [23] were not found necessary for the computation of $\nabla_h I$. The transport is however sensitive to the computation of I_z, which must be consistent with (2.9):

$$(I_z)_{\boldsymbol{i},k} = (dI/d\zeta)_{\boldsymbol{i},k} - \nabla_h I_{\boldsymbol{i},k} \cdot \boldsymbol{u}^I_{\boldsymbol{i},k} \tag{5.8}$$

where $\boldsymbol{u}^I$ in (5.8) denotes the optical flow used to compute the intensity. With I_z computed in this way, the term $-\int_{\hat{Q}} I_z \nabla I \cdot \boldsymbol{\chi} d\boldsymbol{x}dz$ from $F(\boldsymbol{\chi})$ leads with $m_i = n = 0$ in (5.7) to the source term $-(I_z)_{\boldsymbol{i},k} \nabla_h I_{\boldsymbol{i},k}$.

Lumping is implemented as follows for the terms of $\int_{\hat{Q}} \phi'_{\ell-1}[(\nabla \boldsymbol{u}^{\mathrm{T}} + \nabla \boldsymbol{u}) : (\nabla \boldsymbol{\chi}^{\mathrm{T}} + \nabla \boldsymbol{\chi})] d\boldsymbol{x}dz$ from $B(\boldsymbol{u}^{\ell-1}, \boldsymbol{u}, \boldsymbol{\chi})$. In all cases, $n = 0$ in (5.7). Then for diagonal terms, $\phi' \partial_{x_i} u_i \partial_{x_i} \chi_i$, the values $m_j = \delta_{ij}$ are used in (5.7). For off-diagonal terms, $\phi' \partial_{x_i} u_k \partial_{x_\iota} \chi_\kappa$, $i \ne \iota$, $k \ne \kappa$, the values $m_j = \delta_{ij} + \delta_{\iota j}$ are used in (5.7). Also,

$$\beta_{\boldsymbol{i},k} = \phi'\left(\left| [\nabla \boldsymbol{u}^{\mathrm{T}} + \nabla \boldsymbol{u}]^{\ell-1}_{\boldsymbol{i},k} \right|^2 \right) \tag{5.9}$$

is computed using central differences for $\nabla \boldsymbol{u}^{\ell-1}$. Natural one-sided modifications are used at the boundary, and for fractional subscripts β is computed by differencing $\boldsymbol{u}^{\ell-1}$ symmetrically with respect to the appropriate cell face. This lumping is particularly useful to derive the numerical boundary conditions and the resulting stencils are given in detail in [18].

Finally, lumping is implemented for the term $\int_{\hat{Q}} \alpha[\boldsymbol{u}_z \cdot \boldsymbol{\chi}_z] d\boldsymbol{x}dz$ from $B(\boldsymbol{u}^{\ell-1}, \boldsymbol{u}, \boldsymbol{\chi})$ with $m_i = 0$ and $n = 1$ in (5.7), and leads to the standard finite difference discretization of the 1D Laplacian with Neumann boundary conditions.

The discretizations defined above lead to a $2^{Np}K \times 2^{Np}K$ linear system,

$$A_{\ell-1}\boldsymbol{u}^{\ell} = \boldsymbol{f} \tag{5.10}$$

in which the matrix $A_{\ell-1}$ is dependent upon $\boldsymbol{u}^{\ell-1}$. A detailed Taylor series analysis shows that this discretization is consistent with the differential form of the optimality system for the optical flow given in (4.17). According to the following, $\boldsymbol{u}^{\ell}$ is well defined by (5.10).

Theorem 2 *Suppose that the grid values $\{\nabla_h I_{\boldsymbol{i},k}\}$ manifest sufficiently few symmetries that for every $\boldsymbol{a} \in \boldsymbol{R}^N$ and for every skew-symmetric $W \in \boldsymbol{R}^{N\times N}$,*

$$\sum_{\boldsymbol{1}\le \boldsymbol{i}\le 2^p\cdot\boldsymbol{1}} \sum_{1\le k\le K} |\nabla_h I_{\boldsymbol{i},k} \cdot (\boldsymbol{a} + W\mathbf{x}_{\boldsymbol{i}})|^2 > 0, \tag{5.11}$$

unless $\boldsymbol{a} = 0 = W$. Also, assume that $\phi'_{\ell-1}$ is cellwise constant and that (5.9) satisfies $0 < \beta_0 \le \beta_{\boldsymbol{i},k} \le \beta_1 < \infty$. Then $A_{\ell-1}$ in (5.10) is a symmetric and positive definite matrix.

Proof: The matrix is evidently symmetric and non-negative. Suppose there exists a vector of grid values $\boldsymbol{u}^* = \{\boldsymbol{u}^*_{\boldsymbol{i},k}\}$ such that $\boldsymbol{u}^* \cdot A_{\ell-1} \cdot \boldsymbol{u}^* = 0$.

Now let $\boldsymbol{w}$ represent the function which is cellwise constant with respect to $\boldsymbol{x}$ and piecewise linear and globally C^0 with respect to z, and suppose $\boldsymbol{w}$ has coefficients $\{\boldsymbol{u}^*_{\boldsymbol{i},k}\}$ for the corresponding spline tensor products shown in (5.7). Then the terms in $\boldsymbol{u}^* \cdot A_{\ell-1} \cdot \boldsymbol{u}^*$ derived from integrals involving α result from substituting $\boldsymbol{w}$ in these integrals and thus,

$$0 = \boldsymbol{u}^* \cdot A_{\ell-1} \cdot \boldsymbol{u}^* \ge \int_{\hat{Q}} \alpha |\boldsymbol{w}_z|^2. \tag{5.12}$$

Therefore, the coefficients $\{\boldsymbol{u}^*_{\boldsymbol{i},k}\}$ are constant with respect to k.

Now let $\boldsymbol{v}$ represent the function which is cellwise constant with respect to z and piecewise multilinear and globally C^0 with respect to $\boldsymbol{x}$, and suppose $\boldsymbol{v}$ has coefficients $\{\boldsymbol{u}^*_{\boldsymbol{i},k}\}$ for the corresponding spline tensor products shown in (5.7). Then note that the mass matrices for $s^{(0)}(t)$ and $s^{(1)}(t)$, i.e.,

$$M^{(0)} = \left\{ \int_0^1 s^{(0)}(h^{-1}t - k)\, s^{(0)}(h^{-1}t - l)\, dt : \quad 0 \le k, l \le h^{-1} \right\} \tag{5.13}$$

$$M^{(1)} = \left\{ \int_{\frac{h}{2}}^{1-\frac{h}{2}} s^{(1)}(h^{-1}t - k + \tfrac{1}{2})\, s^{(1)}(h^{-1}t - l + \tfrac{1}{2})\, dt : \quad 0 \le k, l \le h^{-1} \right\} \tag{5.14}$$

satisfy the spectral property:

$$\tfrac{1}{6} \boldsymbol{\chi} \cdot M^{(0)} \cdot \boldsymbol{\chi} \le \boldsymbol{\chi} \cdot M^{(1)} \cdot \boldsymbol{\chi} \le \boldsymbol{\chi} \cdot M^{(0)} \cdot \boldsymbol{\chi}. \tag{5.15}$$

Therefore, all terms in $\boldsymbol{u}^* \cdot A_{\ell-1} \cdot \boldsymbol{u}^*$ derived from integrals involving $\phi'_{\ell-1}$ can be estimated in terms of tensor products of splines in (5.7) with $m_i = 1$ and $n = 0$. Thus, all such terms result from substituting $\boldsymbol{v}$ in the corresponding integrals and hence:

$$0 = \boldsymbol{u}^* \cdot A_{\ell-1} \cdot \boldsymbol{u}^* \ge \beta_0 \int_{\hat{Q}} |\nabla \boldsymbol{v}^{\mathrm{T}} + \nabla \boldsymbol{v}|^2 d\boldsymbol{x} dz. \tag{5.16}$$

Since the coefficients $\{\boldsymbol{u}^*_{\boldsymbol{i},k}\}$ are constant with respect to k, $\boldsymbol{v}$ has the form $\boldsymbol{u}^*_{\boldsymbol{i},k} = \boldsymbol{v}(\mathbf{x}_{\boldsymbol{i}}, \mathrm{z}_k) = \boldsymbol{a} + W\mathbf{x}_{\boldsymbol{i}}$ for some $\boldsymbol{a} \in \boldsymbol{R}^N$ and for some skew-symmetric $W \in \boldsymbol{R}^{N\times N}$, as argued in the proof of Theorem 1.

Finally, since $\boldsymbol{u}^* \cdot A_{\ell-1} \cdot \boldsymbol{u}^*$ majorizes the sum in (5.11), that sum must vanish. However, this violates the assumption on I unless $\boldsymbol{u}^* = 0$. ■

The computation of the optical flow can now be summarized as follows:

- Compute $\nabla_h I$ by central differences and I_z by (5.8).
- Set $\boldsymbol{u}^0 = \boldsymbol{u}$ and $\ell = 1$.

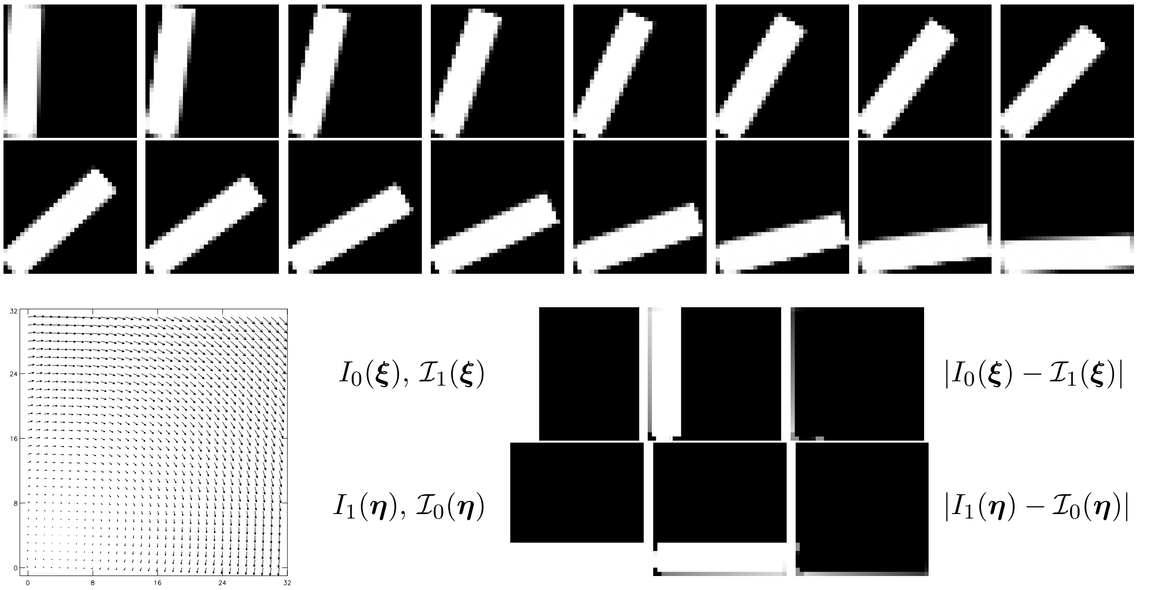

Figure 7: In the two uppermost rows, the intermediate 32×32 images $\{\{I_{\boldsymbol{i},k}\} : 1 \leq k \leq 16\}$ are read from left to right and from top to bottom. The essentially z-independent computed optical flow field is shown in the lower left. The registration error is represented in the lower right, where $I_0(\boldsymbol{\xi})$, $\mathcal{I}_1(\boldsymbol{\xi})$, and $|I_0(\boldsymbol{\xi}) - \mathcal{I}_1(\boldsymbol{\xi})|$, respectively, appear in the top row, and $I_1(\boldsymbol{\eta})$, $\mathcal{I}_0(\boldsymbol{\eta})$, and $|I_1(\boldsymbol{\eta}) - \mathcal{I}_0(\boldsymbol{\eta})|$, respectively, appear in the bottom row.

- Repeat until the relative difference in $\boldsymbol{u}^\ell$ is sufficiently small:
    - ○ Assemble $A_{\ell-1}$ using $\boldsymbol{u}^{\ell-1}$, solve (5.10) for $\boldsymbol{u}^\ell$, and set $\ell = \ell + 1$.
- Set $\boldsymbol{u} = \boldsymbol{u}^\ell$.

According to Theorem 2, the system in (5.10) can be solved using a conjugate gradient method. Although conjugate gradient is relatively slow in the present context, it is used in this introductory work for convenience. On the other hand, note that if $\alpha = \infty$ ($\boldsymbol{u}_z = 0$) and $\phi(s) = \beta s$, then (5.10) is ℓ-independent and has the spectral structure of the elasticity approach of [10] in which fast Fourier methods are used. However, particularly for the treatment of natural boundary conditions, the preferred solution procedure for (5.5) involves nonlinear multigrid techniques [14] [31] as well as multi-scale pyramidal strategies in place of the loop shown at the beginning of Section 5. Further numerical details will be reported separately.

6 Computational Results

The final numerical methods defined in the previous section are applied first to test cases and then to magnetic resonance images. First, Fig. 7 shows a simple example in which the given 32×32 images I_0 and I_1, shown to the right of the optical flow vector field, are related by a pure rotation. All the computations reported in this section were performed using the IDL[†] (Interactive Data Language) system. In every example, h and τ are one but can be rescaled in terms of regularization parameters to be consistent with the definition $Q = (0,1)^N$. Also, $I \in [0,1]$ holds in all examples, and white represents $I = 1$ while black represents $I = 0$. In the example of Fig. 7, $\alpha = 10$ and $\phi(s) = \beta s$ with $\beta = 10$. The successful computation of the rotation is evident in the sequence of intermediate images $\{\{I_{\boldsymbol{i},k}\} : 1 \leq k \leq 16\}$ and in the essentially z-independent rotational optical flow field. Now define the transported or morphed

---

[†] See `http://www.rsinc.com/idl/index.asp`.

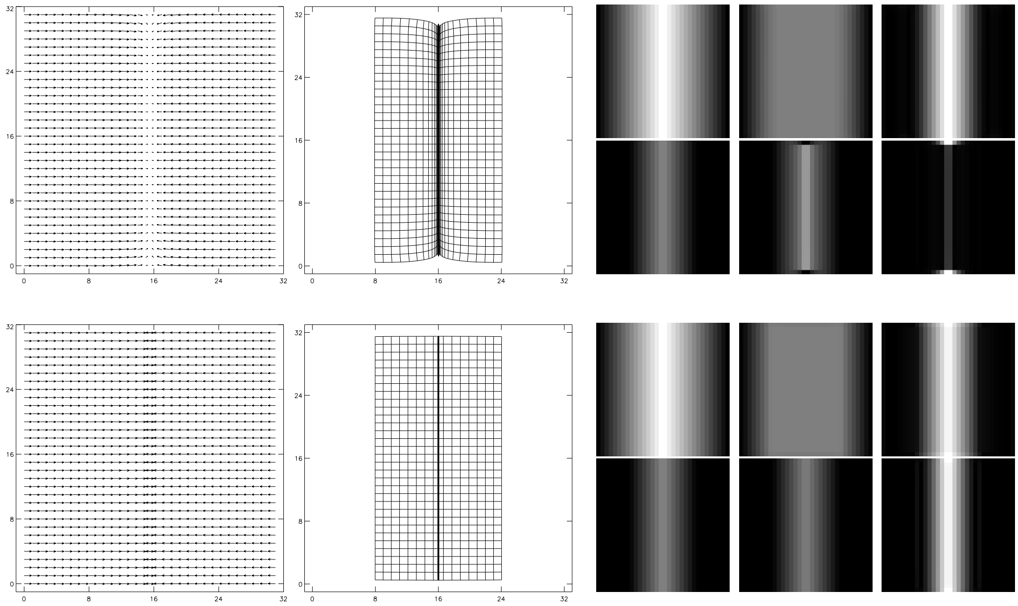

Figure 8: Penalties $\phi(s) = \beta s$ and $\phi(s) = \beta\sqrt{s+\varepsilon}$ are compared in the top and bottom rows, respectively. The essentially k-independent optical flow fields are shown in the left column. The middle column shows the morphing of a uniform grid from Ω_0 to Ω_1. The corresponding registration errors are shown to the right in the same format as used in Fig. 7 but with scaled errors in the rightmost column. Specifically, for each penalty, $I_0(\boldsymbol{\xi})$, $\mathcal{I}_1(\boldsymbol{\xi})$, and $|I_0(\boldsymbol{\xi}) - \mathcal{I}_1(\boldsymbol{\xi})|/E_0^\infty(\Omega_0)$ appear above $I_1(\boldsymbol{\eta})$, $\mathcal{I}_0(\boldsymbol{\eta})$, and $|I_1(\boldsymbol{\eta}) - \mathcal{I}_0(\boldsymbol{\eta})|/E_1^\infty(\Omega_1)$, respectively.

images:

$$\mathcal{I}_0(\boldsymbol{\eta}) = \begin{cases} I_0(\boldsymbol{y}(\boldsymbol{\eta}, 0)), & & \boldsymbol{\eta} \in \Omega_1^{\mathrm{c}}, \\ 0, & \boldsymbol{y}(\boldsymbol{\eta}, \grave{\zeta}) \in \Gamma, & \boldsymbol{\eta} \in \Omega_1^{\mathrm{i}}, \\ I_1(\boldsymbol{\eta}), & \boldsymbol{y}(\boldsymbol{\eta}, \grave{\zeta}) \in \Xi, & \boldsymbol{\eta} \in \Omega_1^{\mathrm{i}} \end{cases} \tag{6.1}$$

$$\mathcal{I}_1(\boldsymbol{\xi}) = \begin{cases} I_1(\boldsymbol{x}(\boldsymbol{\xi}, 1)), & & \boldsymbol{\xi} \in \Omega_0^{\mathrm{c}}, \\ 0, & \boldsymbol{x}(\boldsymbol{\xi}, \acute{\zeta}) \in \Gamma, & \boldsymbol{\xi} \in \Omega_0^{\mathrm{i}}, \\ I_0(\boldsymbol{\xi}), & \boldsymbol{x}(\boldsymbol{\xi}, \acute{\zeta}) \in \Xi, & \boldsymbol{\xi} \in \Omega_0^{\mathrm{i}} \end{cases} \tag{6.2}$$

and the registration errors:

$$E_0^p(\Omega) = \|I_0 - \mathcal{I}_1\|_{L^p(\Omega)}, \qquad \Omega \subseteq \Omega_0, \tag{6.3}$$

$$E_1^p(\Omega) = \|\mathcal{I}_0 - I_1\|_{L^p(\Omega)}, \qquad \Omega \subseteq \Omega_1. \tag{6.4}$$

For the example shown in Fig. 7, the errors satisfy $E_0^1(\Omega_0^{\mathrm{c}}) = 0.0094 = E_1^1(\Omega_1^{\mathrm{c}})$ on the domain subsets on which trajectories extend completely through the full depth of Q, and $E_0^1(\Omega_0) = 0.014 = E_1^1(\Omega_1)$ on the full image domains. Also, $E_0^1(\Omega_0) = 0.016 = E_1^1(\Omega_1)$ holds for the example shown in Fig. 6 for which $\alpha = 1$ and $\beta = 1$ were used. Thus, the approach succeeds to produce a rotation or a translation when one fits the data.

On the other hand, the example shown in Fig. 7 was also constructed so that trajectories emanating from nontrivial pixels in Ω_0 and Ω_1 would impinge on the boundary Γ. As a result, the registration error satisfies $E_0^\infty(\Omega_0^{\mathrm{c}}) = 0.52 = E_1^\infty(\Omega_1^{\mathrm{c}})$ on the subdomains Ω_0^{c} and Ω_1^{c}, but $E_0^\infty(\Omega_0) = 1 = E_1^\infty(\Omega_1)$ on the full domains Ω_0 and Ω_1. By contrast $E_0^\infty(\Omega_0) = 0.45 = E_1^\infty(\Omega_1)$ holds for the translation example shown in Fig. 6. Although the desired registration has been computed for the rotation, there is clearly a potentially influential loss of information when nontrivial trajectories impinge upon Γ, and such a loss can be avoided simply by extending images by zero and using a sufficiently large domain. The alternative use of non-natural boundary conditions would clearly disturb the images shown in Fig. 7.

Next, Fig. 8 shows a computational counterpart to Fig. 3 in which the given 32×32 images I_0 and I_1 are related by an excision, i.e., the middle component $\{I_0 > \frac{1}{2}\}$ is removed to create

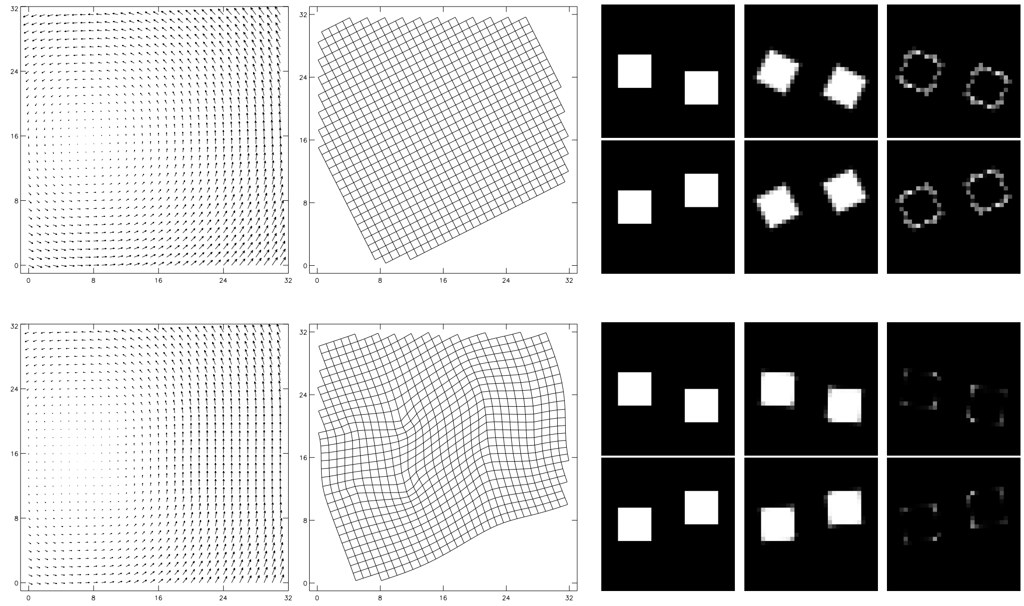

Figure 9: To demonstrate strongly and weakly rigid registration with a simple example, penalties $\phi(s) = \beta s$ with large and small β are compared in the top and bottom rows, respectively. The essentially k-independent optical flow fields are shown in the left column. The middle column shows the morphing of a uniform grid from Ω_0 to Ω_1. The corresponding registration errors are shown to the right in the same format as used in Fig. 7 but with scaled errors in the rightmost column. Specifically, for each penalty, $I_0(\boldsymbol{\xi})$, $\mathcal{I}_1(\boldsymbol{\xi})$, and $|I_0(\boldsymbol{\xi}) - \mathcal{I}_1(\boldsymbol{\xi})|/E_0^\infty(\Omega_0)$ appear above $I_1(\boldsymbol{\eta})$, $\mathcal{I}_0(\boldsymbol{\eta})$, and $|I_1(\boldsymbol{\eta}) - \mathcal{I}_0(\boldsymbol{\eta})|/E_1^\infty(\Omega_1)$, respectively.

I_1. According to the same format used in Fig. 7, I_0 appears above I_1 leftmost among the images shown in Fig. 8. Also, the (Gaussian) penalty $\phi(s) = \beta s$, $\beta = 10^{-3}$, and the (regularized TV) penalty $\phi(s) = \beta\sqrt{s+\varepsilon}$, $\beta = 10^{-4}, \varepsilon = 10^{-2}$ are compared. In both cases, $K = 4$ and $\alpha = 10^5$ are chosen, and the optical flow field is essentially k-independent. The superior performance of the TV penalty can be seen most conspicuously from the middle column in Fig. 8 which shows a morphing of a uniform grid from Ω_0 to Ω_1. Note that for both penalties, the wide grey zone in $\mathcal{I}_1$ shows that the middlemost region of I_1 has been expanded. On the other hand, while the TV penalty maps only greyer pixels in I_0 onto $\mathcal{I}_0$, the Gaussian penalty spuriously maps some brighter pixels of I_0 onto $\mathcal{I}_0$ to generate a brighter strip in the middle of $\mathcal{I}_0$. Also, the inappropriate x_2-dependence resulting from the Gaussian penalty, particularly in the top and bottom image borders, is evident in the corresponding images $\mathcal{I}_0$ and $|I_1 - \mathcal{I}_0|/E_1^\infty(\Omega_1)$. With the Gaussian penalty, the errors are $E_0^1(\Omega_0^c) = 0.14$, $E_0^\infty(\Omega_0^c) = 0.5$, $E_1^1(\Omega_1^c) = 0.011$, and $E_1^\infty(\Omega_1^c) = 0.29$ on the subdomains, and $E_0^1(\Omega_0) = 0.14$, $E_0^\infty(\Omega_0) = 0.5$, $E_1^1(\Omega_1) = 0.013$, and $E_1^\infty(\Omega_1) = 0.5$ on the full domains. With the TV penalty, the errors are $E_0^1 = 0.14$, $E_0^\infty = 0.5$, $E_1^1 = 0.005$, and $E_1^\infty = 0.025$ both on the subdomains and the full domains.

Now, Fig. 9 shows a final simple example to reveal how the strongly rigid registration shown especially in Fig. 7 can be relaxed to what will be referred to as weakly rigid registration obtained by relaxing the dominance of the rigidity penalty. Again, following the format of Figs. 7 and 8, I_0 is shown above I_1 leftmost among the images shown in Fig. 9. Here, the 32×32 images I_0 and I_1 both contain a left-situated square which remains fixed, while a right-situated square moves upward from I_0 to I_1. In both cases of this example, a linear penalty, $\phi(s) = \beta s$, is used and $K = 2$ and $\alpha = 10$ are chosen. The compared cases correspond to $\beta = 10$ (strongly rigid) in the upper part of Fig. 9 and to $\beta = 10^{-2}$ (weakly rigid) in the lower part. The difference between strongly and weakly rigid registration is particularly evident in the respective uniform grid morphings from Ω_0 to Ω_1 shown in the middle column of Fig. 9. Specifically, weakly rigid registration evidently permits a departure from rigidity, i.e., a fluctuation in areas and angles, which vanishes on average and with increasing variance as the dominance of the rigidity penalty is relaxed. The errors corresponding to the strongly rigid case are $E_0^1 = 0.037 = E_1^1$ and $E_0^\infty = 1 = E_1^\infty$ both on the subdomains and the full domains. The errors corresponding to the weakly rigid case are $E_0^1 = 0.0045 = E_1^1$ and $E_0^\infty = 0.41 = E_1^\infty$ both on the subdomains and the full domains. Note that this and other more complex examples were constructed particularly to generate a nonautonomous optical flow field. The field can of course be made nonautonomous for sufficiently small α, but the result manifests more numerical fluctuation than any information rich variation which contributes to the registration. The trend of the flows is toward autonomy, and suggests further investigation of the regularization discussed in Section 3.

Finally, Fig. 10 shows an example of the registration of two magnetic resonance images I_0 and I_1 from a contrast enhanced dynamic scan containing 128×128 pixels each. The scan was performed with a T1-weighted inversion recovery turbo-flash sequence. Again, following the format of Figs. 7 – 9, I_0 is shown above I_1 leftmost among the images shown in Fig. 10. The most conspicuous object in the middle of these images is the left kidney situated to the right of the vertebral column appearing along the left border. This example is similar to that of Fig. 9 in the sense that the left-situated vertebrae remain fixed while the right-situated kidney moves upward from I_0 to I_1 as a consequence of respiration. In both cases of this example, a linear penalty, $\phi(s) = \beta s$, is used and $K = 2$ and $\alpha = 10$ are chosen. As with Fig. 9, the compared cases correspond to $\beta = 10$ (strongly rigid) in the left part of Fig. 10 and to $\beta = 10^{-2}$ (weakly rigid) in the right part. The difference between strongly and weakly rigid registration is again particularly evident in the respective uniform grid morphings from Ω_0 to Ω_1 shown in the middle row of Fig. 10. The errors corresponding to the strongly rigid case are $E_0^1(\Omega_0^c) = 0.046$, $E_0^\infty(\Omega_0^c) = 0.58$, $E_1^1(\Omega_1^c) = 0.046$, and $E_1^\infty(\Omega_1^c) = 0.55$ on the subdomains, and $E_0^1(\Omega_0) = 0.049$, $E_0^\infty(\Omega_0) = 0.61$, $E_1^1(\Omega_1) = 0.048$, and $E_1^\infty(\Omega_1) = 0.62$ on the full domains. The errors corresponding to the weakly rigid case are $E_0^1(\Omega_0^c) = 0.030$, $E_0^\infty(\Omega_0^c) = 0.40$, $E_1^1(\Omega_1^c) = 0.029$, and $E_1^\infty(\Omega_1^c) = 0.44$ on the subdomains, and $E_0^1(\Omega_0) = 0.031$, $E_0^\infty(\Omega_0) = 0.43$, $E_1^1(\Omega_1) = 0.029$, and $E_1^\infty(\Omega_1) = 0.47$ on the full domains. The error images have been displayed according to a common scale, in which 0.64 represents the brightest error intensity, in order to reveal the improvement obtained by the weakly in relation to the strongly rigid registration. Note that these images were taken in sequence after the injection of a Gadolinium-DTPA based contrast agent, as is particularly evident from certain bright spots which appear suddenly in one image and not the other. The registration is particularly difficult in the neighborhood of a bright spot in I_1 situated to the left among the vertebrae, and forthcoming work on image similarity measures will be useful for treating such situations.

References

[1] R.A. Adams, *Sobolev Spaces*, Academic Press, New York, 1975.

[2] A. Borzì, K. Ito and K. Kunisch, *Optimal Control Formulation for Determining Optical Flow*, SIAM J. Sci. Comp. 24(3), pp. 818–847, 2002.

[3] P. Charbonnier, L. Blanc-Féraud, G. Aubert and M. Barlaud, *Deterministic Edge-Preserving Regularization in Computed Imaging*, IEEE Trans. on Image Processing, Vol. 6, No. 2, February 1997.

[4] G.E. Christensen and H.J. Johnson, *Consistent Image Registration*, IEEE Trans. Med. Imaging. Vol. 20, No. 7, July 2001, pp. 568-582.

[5] P.G. Ciarlet, *The Finite Element Method for Elliptic Problems*, North-Holland, Amsterdam, 1978.

[6] P.G. Ciarlet, *Mathematical Elasticity. Volume I: Three-Dimensional Elasticity*, Vol. 20, Studies in Mathematics and its Applications, North-Holland, Amsterdam, 1988.

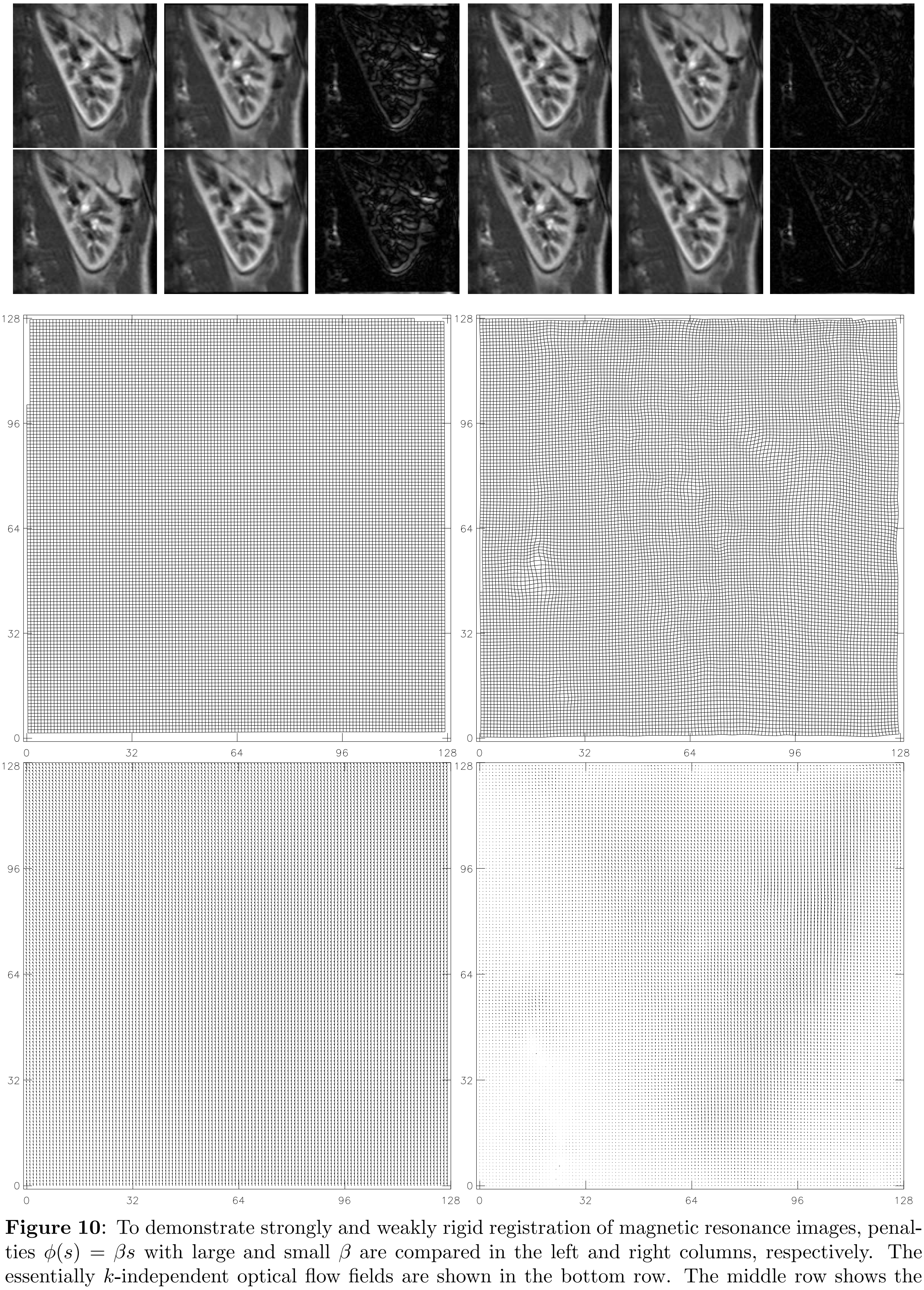

Figure 10: To demonstrate strongly and weakly rigid registration of magnetic resonance images, penalties $\phi(s) = \beta s$ with large and small β are compared in the left and right columns, respectively. The essentially k-independent optical flow fields are shown in the bottom row. The middle row shows the morphing of a uniform grid from Ω_0 to Ω_1. The corresponding registration errors are shown at the top in the same format as used in Fig. 7 but with a common scale for the errors. Specifically, for each penalty, $I_0(\boldsymbol{\xi})$, $\mathcal{I}_1(\boldsymbol{\xi})$, and $|I_0(\boldsymbol{\xi}) - \mathcal{I}_1(\boldsymbol{\xi})|/0.64$ appear above $I_1(\boldsymbol{\eta})$, $\mathcal{I}_0(\boldsymbol{\eta})$, and $|I_1(\boldsymbol{\eta}) - \mathcal{I}_0(\boldsymbol{\eta})|/0.64$, respectively.

[7] P.G. Ciarlet, *Mathematical Elasticity. Volume II: Theory of Plates*, Vol. 27, Studies in Mathematics and its Applications, North-Holland, Amsterdam, 1997.

[8] H.O. Fattorini, *Infinite Dimensional Optimization and Control Theory*, Cambridge University Press, Cambridge, 1999.

[9] B. Fischer and J. Modersitzki, *Curvature Based Image Registration*, J. Math. Imaging and Vision 18, pp. 81–85, 2003.

[10] B. Fischer and J. Modersitzki, *Fast Inversion of Matrices Arising in Image Processing*, Numerical Algorithms 22, pp. 1–11, 1999.

[11] M. Fitzpatrick, D.L.G. Hill and C.R. Maurer, Jr., *Image Registration*, Medical Image Processing, Chapter 8 of Volume II of the Handbook of Medical Imaging, M. Sonka and J.M. Fitzpatrick, ed., SPIE Press (July, 2000).

[12] M. Fitzpatrick, J.B. West and C.R. Maurer, Jr., *Predicting Error in Rigid-Body Point-Based Registration*, IEEE Trans. Med. Imaging, Vol. 17, pp. 694–702, 1998.

[13] S. Haker, A. Tannenbaum and R. Kikinis, *Mass Preserving Mappings and Image Registration*, MICCAI 2001, pp. 120–127.

[14] S. Henn, *Schnelle elastische Anpassung in der digitalen Bildverarbeitung mit Hilfe von Mehrgitterverfahren*, Diplomarbeit Heinrich-Heine-Universität Düsseldorf, 1997.

[15] W. Hinterberger, *Generierung eines Films zwischen zwei Bildern mit Hilfe des optischen Flusses*, Diplomarbeit, Institut für Industriemathematik der Technisch-Naturwissenschaftlichen Fakultät der Johannes Kepler Universität Linz, Linz, Sept 1999.

[16] B.K.P. Horn and B.G. Schunck, *Determining Optical Flow*, Artif. Intell., Vol. 23, pp. 185 – 203, 1981.

[17] S.L. Keeling and R. Bammer, *A Variational Approach to Magnetic Resonance Coil Sensitivity Estimation*, to appear in Appl. Math. Comp.

[18] S.L. Keeling and W. Ring, *Medical Image Registration and Interpolation by Optical Flow with Maximal Rigidity*, SFB Report No. 248, Karl-Franzens-University of Graz, Graz, Austria, May, 2003.

[19] M. Lefébure and L.D. Cohen, *Image Registration, Optical Flow and Local Rigidity*, J. Math. Imaging and Vision, Vol. 14, No. 2, pp. 131–147, March 2001,

[20] J.A. Little, D.L.G. Hill and D.J. Hawkes, *Deformations Incorporating Rigid Structures*, Computer Vision and Image Understanding, Vol. 66, No. 2, pp. 223–232, 1997.

[21] J. Modersitzki, *Habilitation Thesis*, Medizinische Universität Lübeck, 2002.

[22] P.J. Olver, *Applications of Lie Groups to Differential Equations*, Springer, New York, 1986.

[23] S. Osher and L.I. Rudin, *Feature-Oriented Image Enhancement Using Shock Filters*, SIAM J. Numer. Anal., Vol. 27, No. 4, pp. 919 – 940, August 1990.

[24] W. Peckar, C. Schnörr, K. Rohr and H.S. Stiehl, *Parameter-Free Elastic Deformation Approach for 2D and 3D Registration using Prescribed Displacements*, J. Math. Imaging and Vision, Vol. 10, pp. 143–162, 1999.

[25] D. Rueckert, B. Clarkson, D.L.G. Hill and D.J. Hawkes, *Non-rigid Registration using Higher-Order Mutual Information*, Medical Imaging 2000: Image Processing, K. M. Hanson, ed., Proceedings of SPIE, Vol. 3979, pp. 438–447, 2000.

[26] D. Rueckert, L.I. Sonoda, C. Hayes, D.L.G. Hill, M.O. Leach and D.J. Hawkes, *Non-rigid Registration using Free-Form Deformations: Application to Breast MR Images*, IEEE Trans. Med. Imaging, Vol. 18, No. 8, pp. 712–721, 1999.

[27] M.E. Taylor, *Partial Differential Equations: Basic Theory*, Springer, New York, 1996.

[28] J.-P. Thirion, *Image Matching as a Diffusion Process: An Analogy with Maxwell's Demons*, Medical Image Analysis, Vol. 2, No. 3, pp. 243 – 260, 1998.

[29] P.M. Thompson, M.S. Mega, K.L. Narr, E.R. Sowell, R.E. Blanton and A.W. Toga, *Brain Image Analysis and Atlas Construction*, Medical Image Processing, Chapter 17 of Volume II of the Handbook of Medical Imaging, M. Sonka and J.M. Fitzpatrick, ed., SPIE Press (July, 2000).

[30] G.M. Troianiello, *Elliptic differential equations and obstacle problems*, Plenum Press, New York, 1987.

[31] U. Trottenberg, C. Oosterlee and A. Schüller, *Multigrid*, Academic Press, San Diego, 2001.

[32] C.R. Vogel and M.E. Oman, *Iterative Methods for Total Variation Denoising*, SIAM Journal on Scientific Computing, Vol. 17, pp. 227-238, 1996.

[33] J. Weickert, *Anisotropic Diffusion in Image Processing*, B. G. Teubner Stuttgart, 1998.

[34] J. B. West, J. M. Fitzpatrick, M. Y. Wang, B. M. Dawant, C. R. Maurer, Jr., R.M. Kessler, R.J. Maciunas, C. Barillot, D. Lemoine, A. Collignon, F. Maes, P. Suetens, D. Vandermeulen, P.A. van den Elsen, S. Napel, T.S. Sumanaweera, B. Harkness, P.F. Hemler, D.L.G. Hill, D.J. Hawkes, C. Studholme, J.B.A. Maintz, M.A. Viergever, G. Malandain, X. Pennec, M.E. Noz, G.Q. Maguire, Jr., M. Pollack, C.A. Pelizzari, R.A. Robb, D. Hanson and R.P. Woods, *Comparison and Evaluation of Retrospective Intermodality Brain Image Registration Techniques*, J. Comput. Assist. Tomogr., Vol. 21, pp. 554–566, 1997.